JGR Oceans

RESEARCH ARTICLE
10.1029/2019JC015164

Turbulence Observations Beneath Larsen C Ice Shelf, Antarctica

Peter E.D. Davis[1] and **Keith W. Nicholls**[1]

[1]British Antarctic Survey, Natural Environment Research Council, Cambridge, UK

Key Points:
- At the measurement site, the rate of turbulent kinetic energy dissipation is entirely balanced by the rate of shear production
- The under-ice drag coefficient is 0.0022, and the roughness length is 0.44 mm
- The three-equation melt rate model performs well for this example of smooth ice and a cold, unstratified, tidally forced boundary layer

Correspondence to:
P. E. D. Davis,
petvis@bas.ac.uk

Citation:
Davis, P. E. D., & Nicholls, K. W. (2019). Turbulence observations beneath Larsen C ice shelf, Antarctica. *Journal of Geophysical Research: Oceans*, *124*. https://doi.org/10.1029/2019JC015164

Received 20 MAR 2019
Accepted 10 JUL 2019
Accepted article online 16 JUL 2019

Abstract Increased ocean-driven basal melting beneath Antarctic ice shelves causes grounded ice to flow into the ocean at an accelerated rate, with consequences for global sea level. The turbulent transfer of heat through the ice shelf-ocean boundary layer is critical in setting the basal melt rate, yet the processes controlling this transfer are poorly understood and inadequately represented in global climate models. This creates large uncertainties in predictions of future sea level rise. Using a hot-water drilled access hole, two turbulence instrument clusters (TICs) were deployed 2.5 and 13.5 m beneath Larsen C ice shelf in December 2011. Both instruments returned a yearlong record of turbulent velocity fluctuations, providing a unique opportunity to explore the turbulent processes within the ice shelf-ocean boundary layer. Although the scaling between the turbulent kinetic energy (TKE) dissipation rate and mean flow speed varies with distance from the ice shelf base, at both TICs the TKE dissipation rate is balanced entirely by the rate of shear production. The freshwater released by basal melting plays no role in the TKE balance. When the upper TIC is within the log-layer, we derive an under-ice drag coefficient of 0.0022 and a roughness length of 0.44 mm, indicating that the ice base is smooth. Finally, we demonstrate that although the canonical three-equation melt rate parameterization can accurately predict the melt rate for this example of smooth ice underlain by a cold, tidally forced boundary layer, the law of the wall assumption employed by the parameterization does not hold at low flow speeds.

Plain Language Summary Antarctic ice shelves are the floating extensions of the Antarctic ice sheet. They help control the future contribution of Antarctica to global sea level rise by restricting the flow of grounded ice into the ocean. Many ice shelves are increasingly being melted from beneath by relatively warm ocean waters, leading to an acceleration in the flow of ice from the ice sheet interior into the ocean. The very small-scale turbulent processes that control the rate of basal melting, however, are poorly represented in global climate models, resulting in large uncertainties in projections of future sea level rise. Here we present a yearlong record of the turbulent processes that drive basal melting beneath an Antarctic ice shelf. We show that at our measurement site the turbulence generated by the mean flow is dissipated entirely by small-scale molecular processes. The freshwater released by basal melting does not significantly influence the turbulent environment. Most importantly, however, we demonstrate directly from our observations that existing representations of basal melting in global climate models can accurately predict the melt rate when turbulent mixing is sufficiently intense to overcome stratification. Much work remains to be done, as the turbulent environment varies widely between ice shelves.

1. Introduction

Antarctic ice shelves—the floating extensions of the Antarctic ice sheet—play a significant role in global climate. Not only are ice shelf-ocean interactions important for the formation of Antarctic Bottom Water (Foldvik et al., 1985; Foldvik et al., 2004), a major water mass that fills much of the global abyssal ocean, but by retarding the seaward flow of grounded ice from the continental interior (Fürst et al., 2016), ice shelves are also hugely important in regulating Antarctica's contribution to global sea level (Shepherd et al., 2004). The Antarctic cryosphere, however, remains the single largest source of uncertainty in future sea level projections (Church et al., 2013) due to insufficient understanding of some fundamental processes. With some models suggesting Antarctica could contribute >1 m to global mean sea level by 2100 via the marine ice sheet instability (Bamber et al., 2009; DeConto & Pollard, 2016), reducing the uncertainty in the Antarctic ice sheet's future contribution is essential for reliable sea level forecasting.

Antarctic ice shelves are melted from beneath when in contact with ocean waters that have a temperature sufficiently above the in situ freezing point (Jenkins, 1999; Shepherd et al., 2018). The magnitude of basal

melting is controlled by molecular processes at the ice shelf base (McPhee et al., 2008), and the rate at which heat and salt is transported vertically through the turbulent ice shelf-ocean boundary layer (Holland & Jenkins, 1999). Ocean-induced ice shelf thinning can trigger acceleration (Mouginot et al., 2014), thinning (M. McMillan et al., 2014), and mass loss (IMBIE, 2018) from grounded ice upstream, as well as grounding line retreat (Rignot et al., 2014; Scheuchl et al., 2016), with major implications for global sea level rise (Shepherd et al., 2012) and marine ice sheet stability (Bamber et al., 2009). The rate of ocean-induced ice shelf thinning is known to have accelerated over recent decades (Paolo et al., 2015), and mass loss from the Antarctic ice sheet has increased six-fold between 1979-1990 and 2009-2017 (Rignot et al., 2019).

In the Amundsen Sea sector of West Antarctica, warm Circumpolar Deep Water that floods onto the continental shelf (Assmann et al., 2019; Wåhlin et al., 2010; D. P. Walker et al., 2013) can drive rapid melting near ice shelf grounding lines (Jacobs et al., 2011; Khazendar et al., 2016; Pritchard et al., 2012; Shepherd et al., 2002). On Pine Island Glacier, a major outlet glacier in the Amundsen Sea sector that drains ~10% of the West Antarctic Ice Sheet (Shepherd et al., 2001), the turbulent transfer of ocean heat through its channelized ice shelf-ocean boundary layer can drive melt rates of up to 24 m/year away from the grounding line (Stanton et al., 2013). Satellite records indicate that Pine Island Glacier's grounding line has retreated by tens of kilometers since 1992 (Park et al., 2013), and this retreat appears to be part of a longer term trend that was triggered in the 1940s by the creation of a new sub-ice shelf cavity as thinning ice went afloat (Smith et al., 2017). At present, the grounding line may even be engaged in an unstable retreat down the retrograde bedrock slope on which Pine Island Glacier is grounded (Favier et al., 2014; Jenkins et al., 2016). Elsewhere, grounding line retreat on Thwaites Glacier is driving more efficient basal melting (Milillo et al., 2019) and an acceleration in the rate of mass loss from the Amundsen Sea region (IMBIE, 2018).

Over the coming century, model simulations suggest that even the most stable ice shelves, such as Filchner-Ronne, may experience dramatic increases in basal melting as changes in ocean circulation divert warm ocean waters into these historically cold sub-ice shelf ocean cavities (Hellmer et al., 2012, 2017; Timmermann & Hellmer, 2013). Such changes could boost average basal melting beneath Filchner-Ronne from 0.2 m/year to almost 4 m/year during the second half of the 21st century, with implications for global sea level (Hellmer et al., 2012).

Numerous modeling studies have demonstrated that ice shelf basal melting is a critical factor in driving ice sheet retreat (e.g. Arthern & Williams, 2017; Cornford et al., 2015; DeConto & Pollard, 2016; Favier et al., 2014; Goldberg et al., 2019; Joughin et al., 2014), with basal melting near the grounding zone and in the new sub-ice shelf cavities created as melting ice shelves go afloat being particularly important (Arthern & Williams, 2017; Reese et al., 2018; R. T. Walker et al., 2008). Thus, realistic representations of the magnitude and distribution of ice shelf basal melting in global climate models is essential for forecasting 21st century sea level rise. Current parameterizations of basal melting, however, are poorly constrained by observations, and different parameterizations can yield model melt rates that vary by up to a factor of 5 (Dansereau et al., 2014). The canonical three-equation melt rate parameterization (Holland & Jenkins, 1999) has only been calibrated for a single location (Jenkins et al., 2010) and often requires regional tuning to match observed melt rates (Begeman et al., 2018; Dutrieux et al., 2014). Furthermore, the three-equation parameterization is known to perform poorly when predicting the melt rate in the presence of strong stratification (Kimura et al., 2015) or a buoyancy-driven plume flowing along a sloped ice shelf base (McConnochie & Kerr, 2017).

Improving existing parameterizations of basal melting and developing new formulations based on the underlying physics of the turbulent boundary layer is therefore essential for robust global simulations of future sea level rise. Such developments will require both sustained observational and high-resolution modeling studies (e.g., Vreugdenhil & Taylor, 2019) of the different boundary layer environments found beneath a range of Antarctic ice shelves. Here we present a yearlong observational time series of the turbulent environment in the boundary layer beneath an Antarctic ice shelf. Techniques that have been exploited extensively in the Arctic to understand the sea ice-ocean boundary layer (e.g., McPhee, 2002; Peterson et al., 2017) were adapted to provide a unique set of observations that give an unparalleled opportunity to explore the important turbulent processes in a cold, tidally forced sub-ice shelf cavity (Nicholls et al., 2012).

In section 2 we discuss the methods used to observe the ice shelf-ocean boundary layer. In section 3 we present our observations, and in section 4 we develop a turbulent kinetic energy (TKE) budget for the ice shelf-

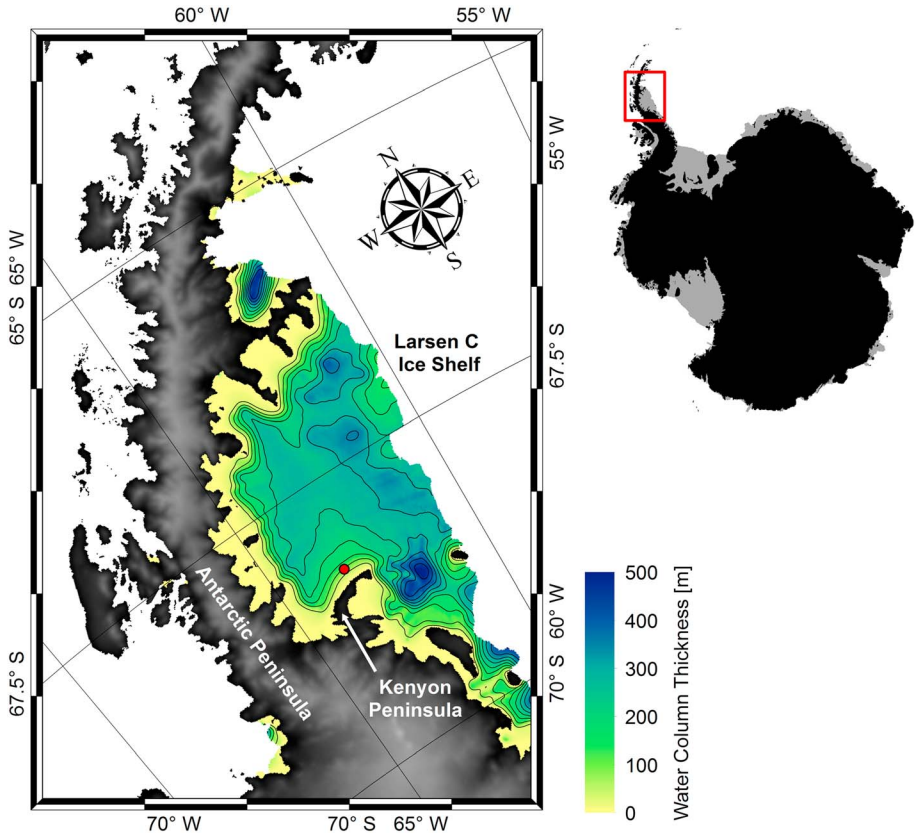

Figure 1. Larsen C ice shelf and the location of the hot water drilled access hole (red dot). Colored contours show water column thickness from Bedmap2 (Fretwell et al., 2013).

ocean boundary layer and discuss the factors that set the scales of turbulence at different depths. We further derive an observational estimate of the drag coefficient and then assess the performance of the canonical three-equation melt rate model. We finish with our conclusions and outlook in section 5.

2. Ice Shelf-Ocean Boundary Layer Observations

2.1. Turbulence Instrument Clusters

An access hole was drilled with hot water through the southern Larsen C ice shelf (68°18.0′S, 63°21.8′W; Figure 1) in December 2011 and used to deploy turbulence instrument clusters (TICs) 2.5 and 13.5 m beneath the ice shelf base (Nicholls et al., 2012; Figure 2a). The ice thickness at the location of the borehole was 355.5 m, the surface elevation 54.5 m, and the sea floor depth 493 m. The water column thickness was 192 m, and the water pressure at the ice shelf base was 304 db. The water column properties at the location of the access hole are relatively uniform (Figures 2b and 2c), with the total range in temperature and salinity not exceeding 0.2°C and 0.05 psu. Below 400 m, and within 25 m of the ice shelf base, the water column is predominantly homogenous, with a density gradient close to zero. The bulk buoyancy frequency at the depth of the TICs is ~3×10^{-4} s^{-1}. A weak pycnocline is seen between 325 and 400 m.

Each TIC was designed to resolve the turbulent fluxes in the ice shelf-ocean boundary layer and consisted of a Nobska Modular Acoustic Velocity Sensor (MAVS) differential acoustic travel-time 3-D velocity sensor and a fast response Rockland Scientific International "MicroSquid" temperature sensor (Figure 2a). A ballast weight was used to hold the flexible mooring cable vertical in the strong tidal currents, and the TICs were directly connected to a data logger at the ice shelf surface. While the Rockland MicroSquid returned a reliable time series of the tidal and longer timescale temperature variability, the very low dynamic range of the turbulent temperature fluctuations in the ice shelf-ocean boundary meant that those signals could not be

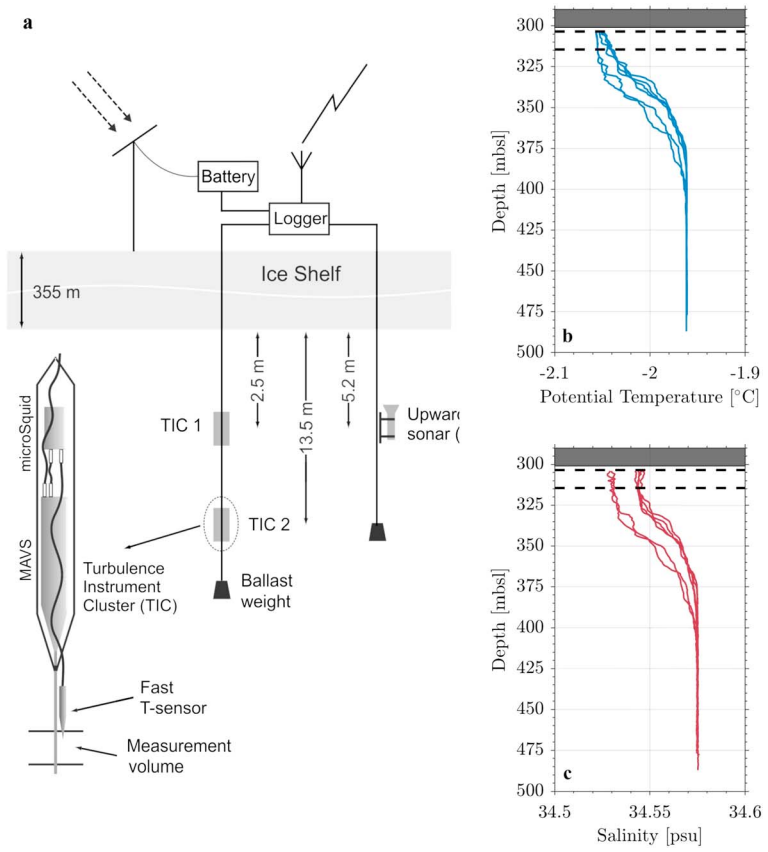

Figure 2. (a) Schematic of the turbulent instrument clusters deployed beneath Larsen C and profiles of (b) potential temperature and (c) salinity at the location of the hot water drilled access hole. The two distinct groups of profiles were taken 7 hr apart, demonstrating the change in water conditions over a tidal cycle. The black dashed lines in (b) and (c) indicate the position of the two turbulence instrument clusters, and the grey patch marks the base of the ice shelf.

resolved by the 10-bit digitizer used to convert the data. The focus of this paper is therefore on the velocity data collected by the MAVS, with each instrument providing a 392-day record of the turbulent velocity fluctuations (Davis & Nicholls, 2019).

The MAVS records four raw path velocities between two sensor rings with an acoustic path length of 9.5 cm (Trivett et al., 1990). These four raw path velocities are mapped into three orthogonal velocity components in an instrument reference frame, with the exact mapping depending on the orientation of the MAVS. Using the pitch, roll, and compass components recorded at the same rate as the velocity, the instrument-frame velocity components are then transformed into a geographically aligned horizontal (u, v) and vertical (w) reference frame. u is defined positive east, v is positive north, and w is positive toward the ice base. The absolute maximum pitch and roll at either MAVS did not exceed 4°, and a magnetic variation correction of 18° east was applied to the horizontal velocity components.

Each MAVS sampled at a rate of 5 Hz and operated in burst mode with 15 min of data collected every two hours. In total, 4,600 bursts were collected. Each individual burst was subjected to a number of quality control checks (fully described in the following sections), and if it failed these checks, excluded from the data set. In total, 286 bursts were flagged as suspect. The 15-min sampling window was chosen as a balance between providing a sample that is long enough to capture the true covariance of the turbulent eddies, while avoiding longer term temporal variability (McPhee, 2008a). Imperfections in the data logging resulted in some variability in the length of each burst; a final burst length of 14.75 min was adopted for use throughout the analysis. Bursts shorter than 14.75 min were excluded from the data set, while only the first 14.75 min of data were used for longer bursts.

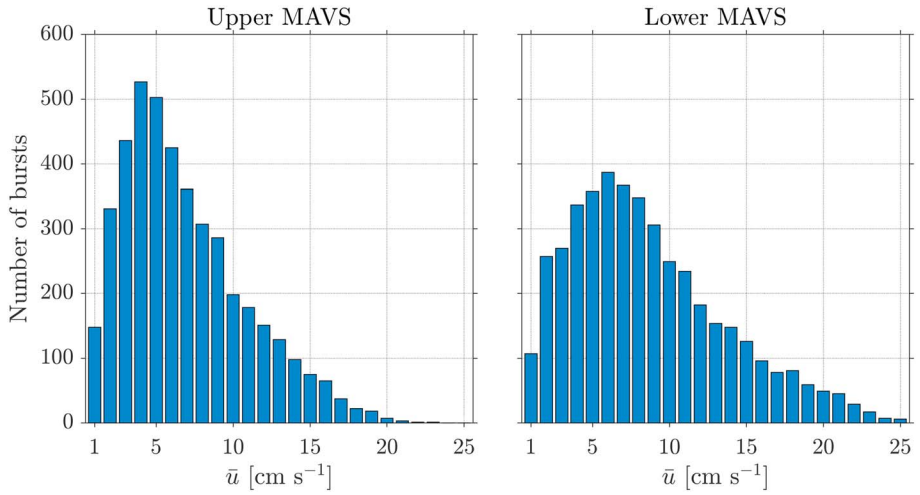

Figure 3. Number of bursts included in each mean flow speed bin for (a) the upper and (b) the lower Modular Acoustic Velocity Sensor (MAVS). At high mean flow speeds (>20 cm/s at the upper MAVS and >23 cm/s at the lower MAVS), the number of bursts included in each bin decreases dramatically, and therefore, the results from these bins should be treated with caution.

2.2. Turbulent Velocity Spectra

Turbulent velocity spectra were calculated using standard methods (McPhee, 2002, 2008a). Initially, the geographically referenced horizontal and vertical velocity components from each burst are rotated into a "streamwise" coordinate system aligned with the mean flow direction during that burst (u_s,v_s,w_s). In this coordinate system, the cross stream and vertical velocity components average to zero ($\overline{v}_s = \overline{w}_s = 0$; where overbar represents the burst average), and $\overline{u}_s$ is equal to the burst averaged flow speed: $\overline{u}_s = \overline{u} = \overline{\sqrt{u^2 + v^2 + w^2}}$. Deviatory time series ($u_s^{'}, v_s^{'}, w_s^{'}$) for each burst are then formed, where, for example, $u_s^{'} = u_s - \overline{u}_s$. From the deviatory time series, the one-sided turbulent velocity energy spectra in frequency space, $E_{jj}(f)$, are computed for each streamwise velocity component, j, using the multitaper method (Thomson, 1982).

Taylor's "frozen field" hypothesis is used to convert frequency space, f, into angular wavenumber space, k (Pope, 2000; Tennekes & Lumley, 1972)

$$k = \frac{2\pi f}{\overline{u}}, \tag{1}$$

and the one-sided turbulent velocity energy spectra in wavenumber space for any velocity component, $E_{jj}(k)$, can be derived from the corresponding one-side energy spectra in frequency space as

$$E_{jj}(k) = 2\pi E_{jj}(f)\overline{u}. \tag{2}$$

The "frozen field" hypothesis is considered valid when the turbulent velocity fluctuations are considerably smaller than the mean velocity, or

$$\frac{u_{s\ \mathrm{RMS}}^{'}}{\overline{u}} \ll 1, \tag{3}$$

where $u_{s\ \mathrm{RMS}}^{'}$ is the root-mean-square of the deviatory time series in the direction of mean advection (Bluteau et al., 2011). Here we use a cutoff of 0.5. Bursts that violate the "frozen field" hypothesis were excluded from the analysis.

To reduce variance at high angular wavenumbers, all wavenumber spectra are bin averaged onto a common $\log_{10}(k)$ grid (McPhee, 2002). To increase the signal-to-noise ratio further, wavenumber spectra from different MAVS bursts are then bin averaged as a function of mean flow speed, with a bin width of 1 cm/s (Figure 3). At high mean flow speeds (>20 cm/s at the upper MAVS and >23 cm/s at the lower MAVS),

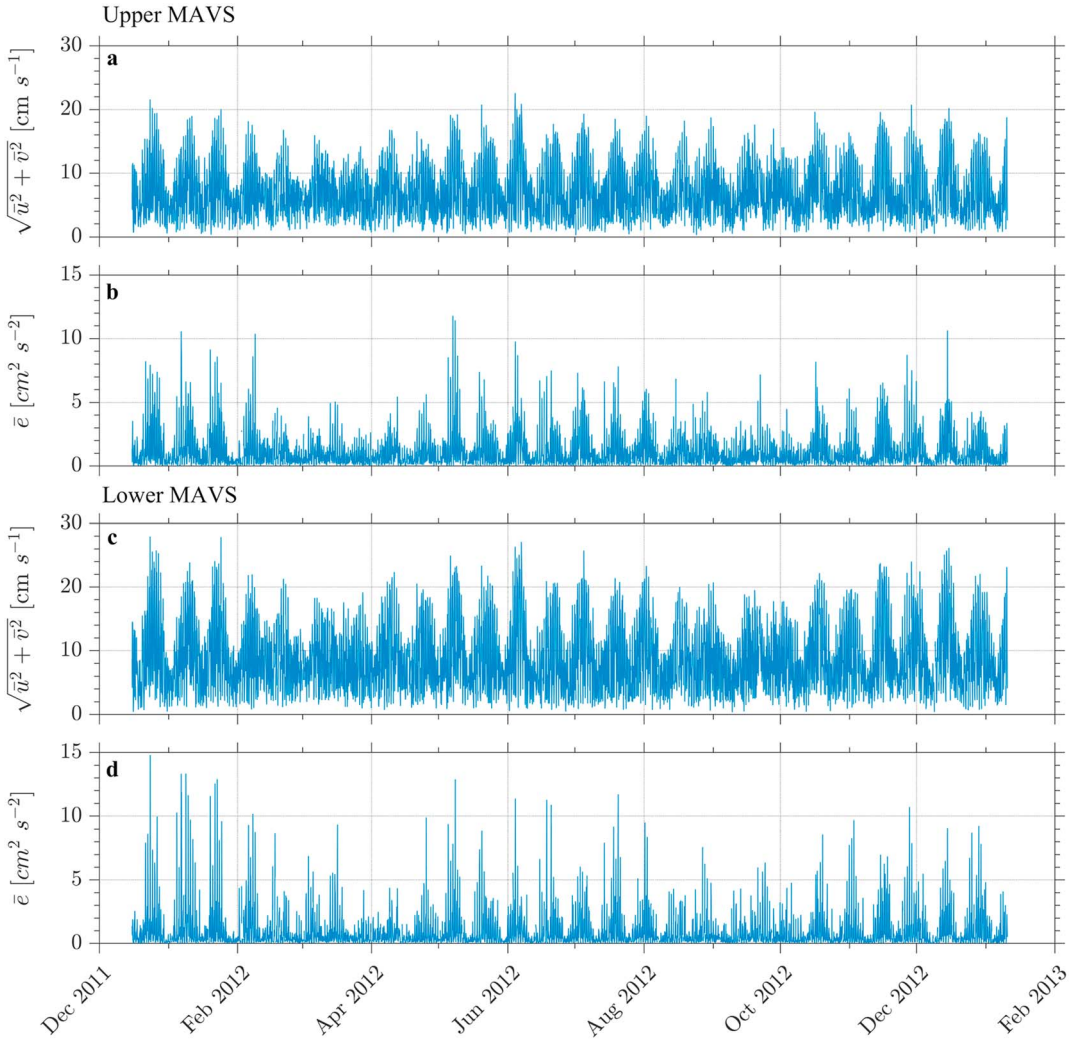

Figure 4. Burst-averaged time series of (a and c) horizontal flow speed and (b and d) turbulent kinetic energy from the upper and lower Modular Acoustic Velocity Sensor (MAVS).

the number of bursts in each bin decreases dramatically, and the results from these bins must be treated with caution. A more typical approach in observational turbulence analysis is to average wavenumber spectra as a function of time during relatively steady flow conditions (McPhee, 2008a). This approach is not possible here due to the strong tidal currents (Figures 4a and 4c). As a result, in this study we do not consider the temporal evolution of the turbulent properties beneath Larsen C.

2.3. TKE Dissipation Rate

Under isotropic conditions, the inertial subrange of the one-sided turbulent velocity energy spectra in wavenumber space for any streamwise velocity component can be used to estimate the TKE dissipation rate, ε (Bluteau et al., 2011)

$$E_{jj}(k) = A_j C \varepsilon^{2/3} k^{-5/3}, \tag{4}$$

where $C = 1.5$ is the empirical Kolmogorov universal constant and A_j is a constant that depends on the velocity component used to derive the wavenumber spectrum (Pope, 2000). In the direction of the mean flow $A_u = 18/55$. In the cross stream and vertical directions $A_v = A_w = 1.33A_u$ (Pope, 2000).

To calculate the rate of TKE dissipation as a function of mean flow speed, equation (4) is fitted to the mean turbulent velocity wavenumber spectrum from each mean flow speed bin for each streamwise velocity component after the noise floor has been subtracted (see Appendix A; J. M. McMillan et al., 2016). The fit is

computed in log space over all possible quarter-wavenumber decades, and the TKE dissipation rate associated with the quarter-wavenumber fit with the lowest root-mean-square deviation from the observed spectrum is extracted.

In a stratified fluid, the inertial subrange is restricted to length scales between the Ozmidov length scale

$$L_O = \left(\frac{\varepsilon}{N^3}\right)^{1/2}, \tag{5}$$

where N is the buoyancy frequency and the Kolmogorov length scale

$$L_K = \left(\frac{\nu^3}{\varepsilon}\right)^{1/4}, \tag{6}$$

where ν is the kinematic viscosity of seawater (Pope, 2000). To confirm that the best fit quarter-wavenumber decade lies within the inertial subrange, the rate of TKE dissipation associated with this fit is used to calculate the theoretical wavenumber bounds $3/L_O \leq k \leq 1/(10L_K)$ of the inertial subrange (Bluteau et al., 2011). If the best fit quarter-wavenumber decade falls outside the inertial subrange, an iterative process is used to find the rate of TKE dissipation associated with the quarter-wavenumber decade that has the lowest root-mean-square deviation from the observed spectrum while satisfying the theoretical wavenumber bounds.

2.4. Friction Velocity and Mixing Length

Alongside the turbulent velocity spectra and the rate of TKE dissipation, two further turbulent quantities are derived: friction velocity and mixing length. Friction velocity is a measure of the overturning speed of the large, energy containing eddies, and the mixing length represents the vertical distance over which they diffuse momentum (McPhee, 1994). For each MAVS burst, friction velocity is calculated as a function of the burst-averaged kinematic Reynolds stresses, $\overline{u_s' w_s'}$ and $\overline{v_s' w_s'}$:

$$u_* = \left[\overline{u_s' w_s'}^2 + \overline{v_s' w_s'}^2\right]^{\frac{1}{4}}. \tag{7}$$

Both the MAVS central strut and the flexible mooring on which they were deployed (Figure 2a) create noise in the covariance terms that artificially increase the magnitude of the friction velocity. Therefore, the deviatory velocity time series are filtered prior to calculating the covariance terms (Appendix A). The individual estimates of friction velocity are subsequently bin averaged as a function of mean flow speed such that they are comparable with the estimates of the TKE dissipation rate. Note that the definition of the friction velocity in equation (7) is local to the depth of each MAVS, rather than that at the ice shelf base (McPhee, 2002).

Mixing length is estimated from the inverse of the wavenumber at the peak of the variance-preserving form of the streamwise vertical velocity turbulent wavenumber spectrum: $k.E_{w_s w_s}(k)$ (McPhee, 1994; McPhee & Martinson, 1994). To calculate the mixing length, the variance-preserving vertical velocity spectra are first derived for each individual MAVS burst. Following the same approach discussed above for the turbulent velocity spectra, the individual variance-preserving spectra are then averaged onto a common $\log_{10}(k)$ grid, before being bin averaged as a function of mean flow speed. For each mean flow speed bin, a least squares spline curve is fitted to the mean variance-preserving spectrum (McPhee, 2008a), and the angular wavenumber at the peak of this curve ($k_{\max}$) is extracted. Mixing length is subsequently calculated as (McPhee, 1994):

$$\lambda_m = \frac{0.85}{k_{\max}}. \tag{8}$$

2.5. CTD Profiles and Upward Looking Sonar

Concurrent with the deployment of the TICs, snapshots of the water column structure beneath Larsen C were obtained with a FastCat SBE49 CTD (conductivity-temperature-depth) sensor. The temperature and salinity are estimated to have an accuracy of 0.004°C and 0.005 psu. A second hot-water drilled access hole located at the same site was instrumented with an upward looking sonar (ULS; Figure 2a). An estimate of the rate of basal melting at the TICs can be derived from the time derivative of the range from the ULS to the ice shelf base (Nicholls et al., 2012). As the ULS was deployed on a flexible cable, the range estimates are contaminated at tidal frequencies by swinging of the mooring line. This noise was removed by low-pass filtering the range estimates with a cutoff at 15 days, and the melt rate was subsequently calculated from the time derivative of this smoothed time series.

Table 1
Ellipse Parameters for the Seven Strongest Tidal Constituents at the Upper and Lower MAVS

	Upper MAVS			
Constituent	Semimajor (cm/s)	Semiminor (cm/s)	Phase (°)	Inclination (°)
P1	1.81	+0.14	324	154
K1	5.47	+0.45	322	154
O1	4.69	+0.61	294	154
K2	1.03	-0.56	234	143
M2	5.33	-1.26	343	1
S2	3.89	-0.92	12	4
N2	0.75	-0.14	324	2
	Lower MAVS			
Constituent	Semimajor (cm/s)	Semiminor (cm/s)	Phase (°)	Inclination (°)
P1	2.52	+0.01	328	155
K1	7.44	+0.76	325	152
O1	6.75	+1.19	295	147
K2	1.48	-0.38	232	150
M2	6.24	-1.10	345	3
S2	4.60	-0.44	17	0
N2	0.92	-0.23	326	3

Note. Inclination angles are defined positive counterclockwise from due east.
Abbreviation: MAVS, Modular Acoustic Velocity Sensor.

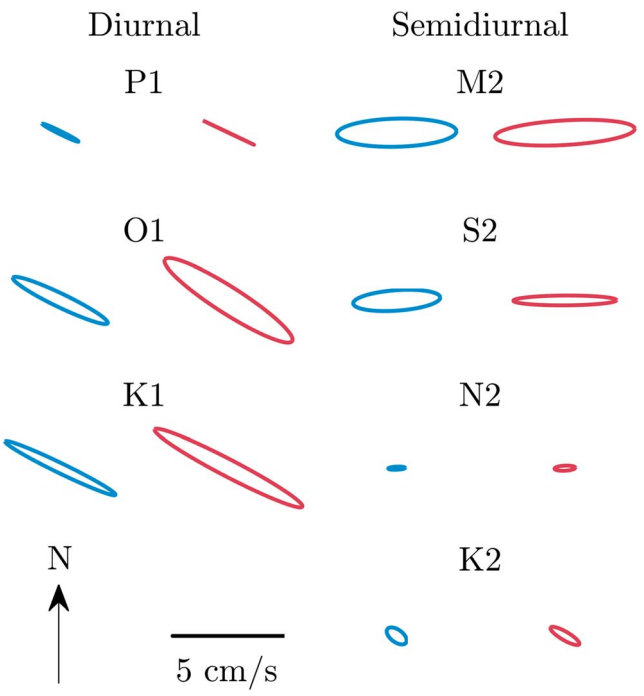

Figure 5. Tidal ellipses for the seven major tidal constituents from the upper (blue) and lower (red) Modular Acoustic Velocity Sensor.

3. Results

Here we present our observations of the turbulent environment beneath Larsen C. In section 4 we then combine these different observations to explore the dynamics of the ice shelf-ocean boundary layer in more detail.

3.1. Burst-averaged Flow Speed and TKE

Consistent with the analysis of Nicholls et al. (2012) from the same site, the horizontal flow at both the upper and lower MAVS is dominated by the tides (Figures 4a and 4c). The maximum burst-averaged flow speed at the upper MAVS (22.6 cm/s) is weaker than that at the lower MAVS (27.9 cm/s), commensurate with its proximity to the ice shelf base. Harmonic analysis (Codiga, 2011) of the burst-averaged velocity time series shows that the tides have mixed diurnal and semidiurnal properties. The ellipse parameters for the seven strongest constituents (three diurnals and four semidiurnals) are given in Table 1 and Figure 5. Semidiurnal tidal currents are broadly aligned east-west, in line with the geographic orientation of the Kenyon Peninsula (Figure 1), while the diurnal tidal ellipses are largely orientated northwest-southeast. The negative semidiurnal semiminor axes (counterclockwise rotation of the tidal current vector with time; Table 1) are consistent with the effect of friction against the ice shelf base (e.g., Makinson et al., 2006; Prandle, 1982). The amplitude of the tides (i.e., the semimajor axis) presented in Table 1 differ substantially from those reported by Nicholls et al. (2012). Nicholls et al. used the response method to extract the ellipse parameters from an 8-day time series, and thus the discrepancies are likely related to the length of the time series and aliasing of the spring-neap cycle. Note that the ellipse parameters presented here should be used in preference to those from Nicholls et al. in future studies.

The intensity of the turbulence within the ice shelf-ocean boundary layer, quantified through the burst-averaged TKE

$$\overline{e} = \frac{1}{2}\left[\overline{\left(u_s'\right)^2} + \overline{\left(v_s'\right)^2} + \overline{\left(w_s'\right)^2}\right], \tag{9}$$

is also dominated by the tides and shows a clear spring-neap cycle at both MAVS (Figures 4b and 4d). During neap tides, the TKE averages 1 to 2 cm^2/s^2 but increases by up to an order of magnitude (>10 cm^2/s^2) during spring tides (especially at the lower MAVS), as a vigorous turbulent eddy field in the ice shelf-ocean boundary layer drives elevated levels of TKE. While the spring tide peaks in TKE are greater at the lower MAVS than at the upper MAVS, the median TKE and 75th percentile for the whole deployment are greater at the upper MAVS than at the lower MAVS (0.7 and 1.4 cm^2/s^2 compared with 0.4 and 1.0 cm^2/s^2). On longer time scales, the interaction of the diurnal and semidiurnal tides generates periods of elevated (e.g., June 2012 or December 2012) and reduced (e.g., April 2012 or September 2012) TKE associated with modulation of the tidal current strength.

3.2. Wavenumber Spectra and TKE Dissipation Rate

Turbulent velocity wavenumber spectra as a function of mean flow speed for the along-stream and vertical velocity components all show a clear inertial subrange spanning at least two wavenumber decades (Figure 6). In the inertial subrange, the ratios between the along-stream and vertical cross-stream velocity spectra lie within the theoretical range of 1 to 4/3 (not shown), indicating that at these scales the turbulence in the ice shelf-ocean boundary layer is largely isotropic (Batchelor, 1976; Biltoft, 2001; Chamecki

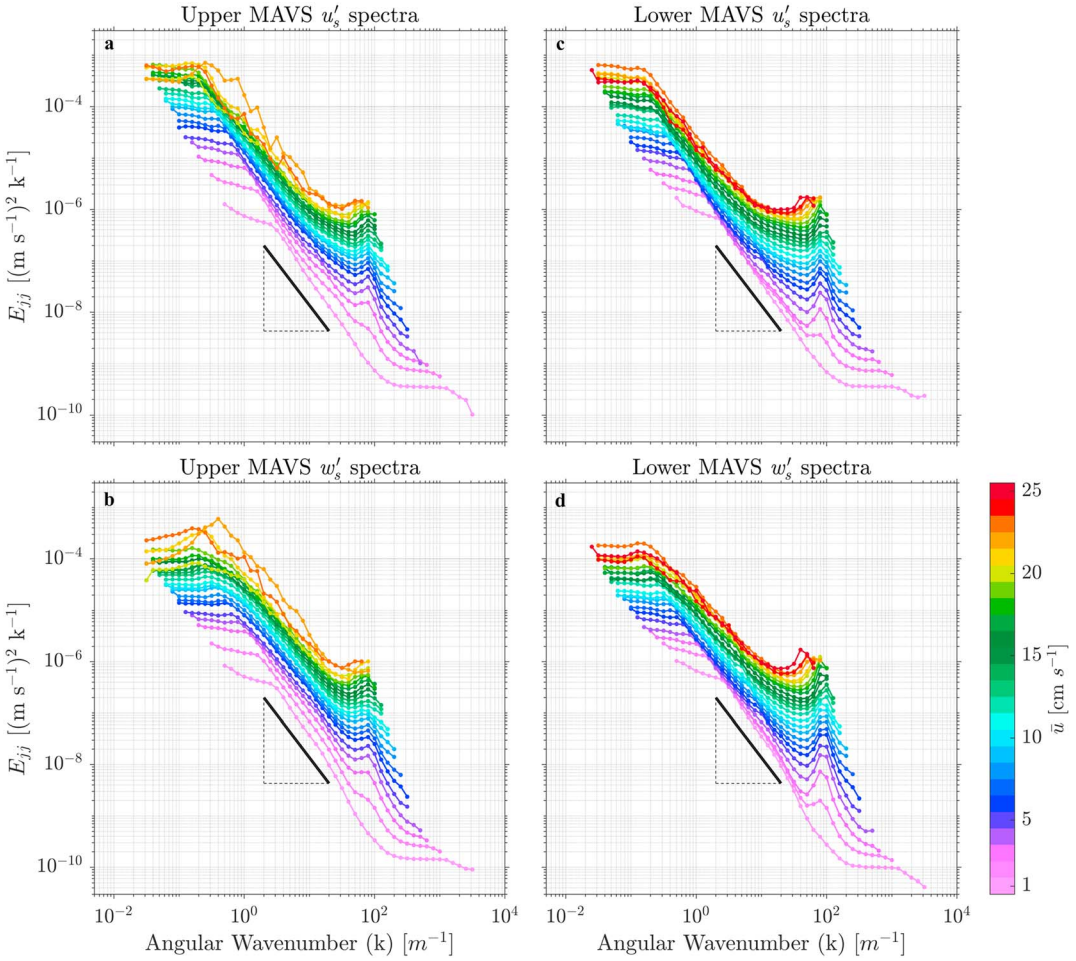

Figure 6. Turbulent velocity wavenumber spectra as a function of mean flow speed for (a and b) the upper and (c and d) the lower Modular Acoustic Velocity Sensor (MAVS). Shown here are spectra for (a and c) the along-stream velocity component and (b and d) the vertical cross-stream velocity component. The thick black line in each panel is a representative -5/3 slope. The eddy shed from the MAVS central strut is clearly visible at $k = 10^2$ m^{-1}. Spectra from the horizontal cross-stream velocity component are not shown but have a shape similar to the vertical cross-stream spectra.

& Dias, 2004; Tennekes & Lumley, 1972). At smaller wavenumbers outside of the inertial subrange, and in the area of the wavenumber spectra contaminated by the eddy shed from the MAVS central strut, the ratio changes significantly and the turbulence at these scales is clearly anisotropic (Batchelor, 1976).

For all turbulent velocity spectra (Figure 6), the power spectral density at any wavenumber increases as a function of mean flow speed at both MAVS, reflecting the elevated levels of TKE observed during the periods of strongest tidal flow (Figure 4). For a given mean flow speed, the energy level at the upper MAVS is greater than that at the lower MAVS, mirroring the higher median TKE observed at the upper MAVS. At the highest mean flow speeds, the quality of the wavenumber spectra deteriorate due to the limited number of bursts included in these mean flow speed bins (Figure 3).

In line with the increasing energy levels as a function of mean flow speed, the rate of TKE dissipation increases from a minimum of ~10^{-9} W/kg at both MAVS to a maximum of ~10^{-6} W/kg at the upper MAVS and ~10^{-7} W/kg at the lower MAVS (Figures 7a and 7b). The rate of TKE dissipation is similar to that observed under sea ice in the Arctic (McPhee, 2002; Peterson et al., 2017) and the Antarctic (McPhee, 1994; McPhee & Martinson, 1994), but is greater than that observed beneath Pine Island Ice Shelf (~10^{-9} W/kg; Kimura et al., 2016) and George VI Ice Shelf (~10^{-10} W/kg; Venables et al., 2014). As a function of mean flow speed, ε scales as a power law at the upper MAVS ($r^2 = 0.93$) and exponentially at the lower MAVS ($r^2 = 0.93$). For mean flow speeds above 10 cm/s at the upper MAVS, ε scales closely with the cube of the mean flow speed ($r^2 = 0.78$). The significance of this cubic scaling is discussed later in section 4.2.

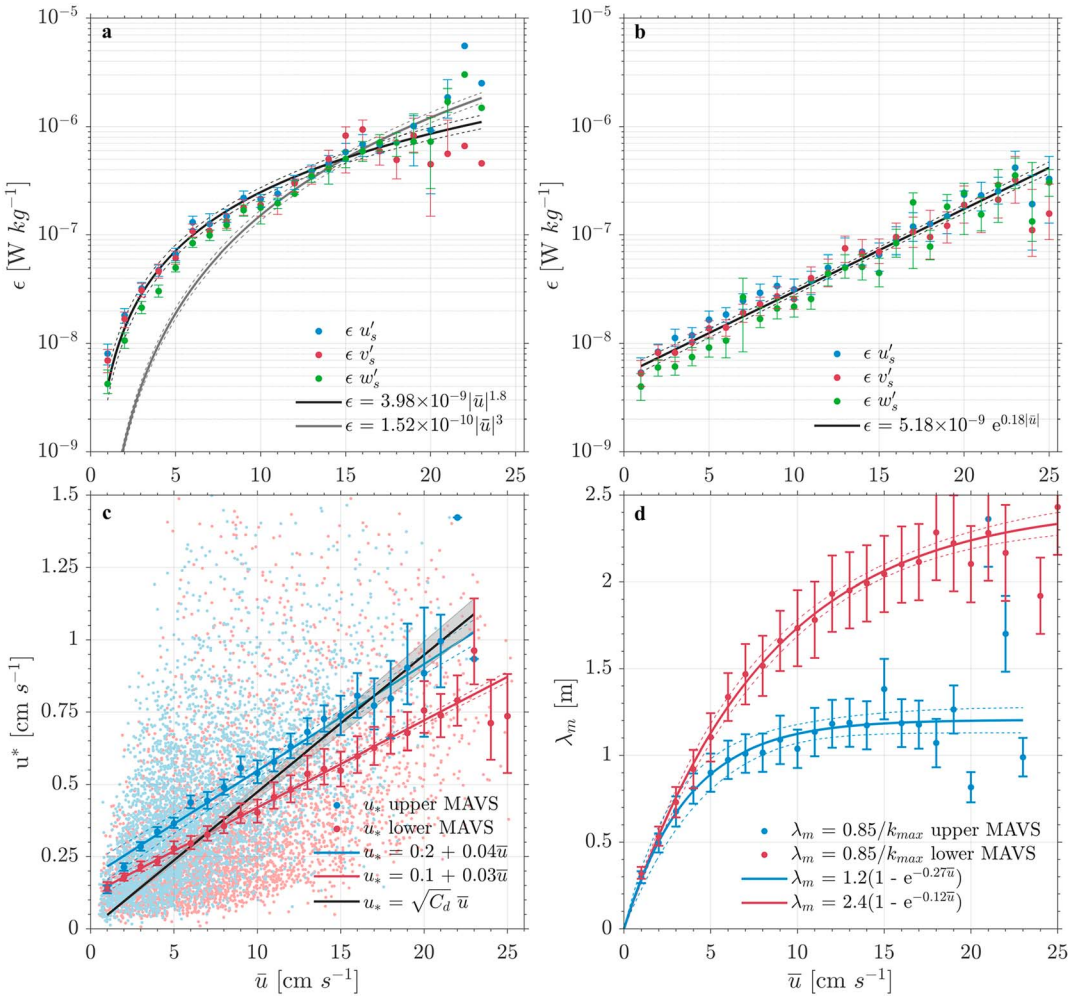

Figure 7. (a) Rate of turbulent kinetic energy dissipation, ε, at the upper Modular Acoustic Velocity Sensor (MAVS) derived from the along-stream and cross-stream turbulent velocity wavenumber spectra. The black solid line is a power-law fit to ε over all mean flow speed bins. The grey line is a cubic power-law fit to ε for mean flow speeds greater than 10 cm/s. (b) The same as (a) except for the lower MAVS. The black solid line is an exponential fit to ε over all mean flow speed bins. (c) Friction velocity as a function of mean flow speed (large colored dots) from the upper (blue) and lower (red) MAVS. The small blue and red dots are the average friction velocity from each individual MAVS burst. The solid blue and red lines are linear fits to the bin-averaged friction velocity. The solid black line is an estimate of the friction velocity derived from the drag coefficient (see section 4.3). The grey patch represents the uncertainty in the drag coefficient. (d) Mixing length as a function of mean flow speed from the upper (blue) and lower (red) MAVS. The solid blue and red lines are asymptotic exponential growth fits to the bin-averaged mixing length.

3.3. Friction Velocity and Mixing Length

Friction velocity (Figure 7c) shows a large scatter, with values ranging from 0.01 to 2.7 cm/s. The scatter is related to the length of each burst and the balance that must be struck between sampling long enough to capture the true covariance of the turbulent eddy field while avoiding longer term temporal variability. In some cases, the length of each burst is too short to fully capture the eddy covariance, resulting in a large spread of friction velocities. Like the rate of TKE dissipation, friction velocities beneath Larsen C are similar to those found in neutral boundary layers beneath Arctic and Antarctic sea ice (McPhee, 2008b; Peterson et al., 2017), but somewhat less than those observed in the channelized ice shelf-ocean boundary layer beneath Pine Island Glacier (Stanton et al., 2013). Friction velocity scales linearly with mean flow speed at both MAVS, and its magnitude is generally greater at the upper MAVS, consistent with higher Reynolds stresses closer to the boundary.

At low-flow speeds, differing behavior is observed between the upper and lower MAVS. While friction velocity at the upper MAVS begins to decrease faster than the linear scaling suggests for mean flow speeds below

3 cm/s, no such behavior is observed at the lower MAVS. The large scatter in individual estimates of the friction velocity means that more observations at these flow speeds would be required to understand these differences in behavior in more detail and to address questions related to minimum friction velocities appropriate for use in models (e.g., Gwyther et al., 2015).

At both MAVS, mixing length increases with mean flow speed from a minimum of 0.3 m (Figure 7d). At the upper MAVS, the mixing length asymptotes towards a maximum of ≈1.2 m above $\overline{u} = 10$ cm/s. At the lower MAVS, the maximum observed mixing length ranges between 2 and 2.5 m. Larger mixing lengths at the lower MAVS are consistent with its greater distance from the ice shelf base. As distance to the boundary increases, the presence of the boundary exerts less of a restriction on the size of the energy-containing eddies. The size of the mixing length at the depth of each MAVS is consistent with observations at similar depths under Arctic and Antarctic sea ice (McPhee, 2002; McPhee & Martinson, 1994). The physical processes that set the mixing length will be discussed in the section 4.2.

4. Discussion

In this section, we use our observations of the turbulent environment beneath Larsen C to explore the dynamics of the boundary layer in more detail. In particular, we develop a TKE budget for the ice shelf-ocean boundary layer, discuss the processes that set the scales of turbulence, derive an estimate of the under-ice drag coefficient, and quantify the performance of the canonical three-equation melt rate model.

4.1. TKE Budget

Successful parameterizations of basal melting must be sensitive to the range of different turbulent environments found beneath Antarctic ice shelves. For example, basal melt rates predicted by the three-equation parameterization beneath George VI ice shelf are an order of magnitude higher than observations (Kimura et al., 2015), and this discrepancy is likely related to the inability of the three-equation parameterization to account for the effects of buoyancy on the intensity of the turbulence. Here we derive an observational estimate of the TKE budget beneath Larsen C, highlighting the important sources and sinks of turbulence in the ice shelf-ocean boundary layer.

For a steady stratified shear flow that is horizontally homogenous with no mean vertical motion, the TKE equation in the ice shelf-ocean boundary layer is given by (McPhee, 2008a; Tennekes & Lumley, 1972)

$$-\langle u'w'\rangle\frac{\partial\overline{u}}{\partial z}-\langle v'w'\rangle\frac{\partial\overline{v}}{\partial z}-\frac{g}{\rho_w}\langle\rho_w^{'}w^{'}\rangle=\frac{\partial}{\partial z}\left(\frac{\langle u_i^{'}u_i^{'}w^{'}\rangle}{2}+\frac{\langle p'w'\rangle}{\rho_w}\right)+\nu\left\langle\left(\frac{\partial u_i^{'}}{\partial x_j}+\frac{\partial u_j^{'}}{\partial x_i}\right)\frac{\partial u_j^{'}}{\partial x_i}\right\rangle, \tag{10}$$

where z is depth, p is pressure, ν is viscosity, $\langle\ \rangle$ indicates a time average, and i and j are Einstein notation indices. A cross-correlation analysis (not shown) indicates that there is no lag between the burst averaged TKE and mean flow speed (Figure 4), justifying the use of a steady state TKE equation. The first two terms on the left-hand side represent the rate of TKE production by the turbulent Reynolds stresses acting against the mean shear

$$P_s=-\langle u'w'\rangle\frac{\partial\overline{u}}{\partial z}-\langle v'w'\rangle\frac{\partial\overline{v}}{\partial z}, \tag{11}$$

while the third term on the left-hand side is the production rate of TKE through buoyancy (gravitational) forces, b, in the fluid

$$P_b=-\frac{g}{\rho_w}\langle\rho_w^{'}w^{'}\rangle=-\langle w'b'\rangle. \tag{12}$$

To explain the signs in equation (12), we note that if the TKE buoyancy production rate, P_b, is positive, positive density anomalies are moving away from the ice base and energy is added to the turbulence by gravity (i.e., convection; negative $\langle w^{'}b^{'}\rangle$). In contrast, if the TKE buoyancy production rate is negative, positive density anomalies are moving toward the ice base (i.e., positive $\langle w^{'}b^{'}\rangle$), and energy is being expended moving denser fluid upward (McPhee, 2008a).

The first term on the right-hand side represents the vertical component of the TKE transport, consisting of the divergence of the vertical flux of TKE and the covariance of the vertical velocity with the turbulent pressure fluctuations. The second term on the right-hand side is the rate of TKE dissipation, ε, into internal

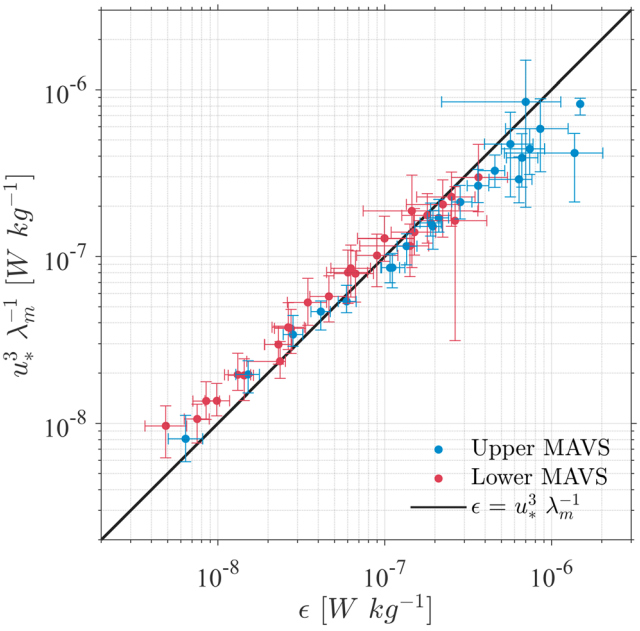

Figure 8. Rate of turbulent kinetic energy dissipation, ε, plotted against the rate of shear production of turbulent kinetic energy, P_s, calculated as a function of the observed friction velocity and mixing length. The black line marks the one-to-one relationship between P_s and ε.

energy (heat) of the fluid through viscous processes. The vertical component of the TKE transport term is a challenging quantity to observe in the field. Nevertheless, although the vertical velocity pressure covariance is not measured by our instruments, a finite-difference approximation of the divergence of the vertical flux of TKE can be made for the mid-point between the upper and lower MAVS (McPhee, 2004)

$$D = \frac{\partial}{\partial z}\left(\frac{\langle w' u_i' u_i' \rangle}{2}\right) \approx \frac{\langle w'e' \rangle_L - \langle w'e' \rangle_U}{22}, \tag{13}$$

where $\langle w'e' \rangle = \langle w' u_i' u_i' \rangle$ and the subscripts U and L indicate the upper and lower MAVS, respectively. The sign of D varies in time, with a median value of -6.07×10^{-12} W/kg and an interquartile range of -2.61×10^{-9} W/kg to 3.38×10^{-9} W/kg. This is an order of magnitude smaller than the estimates of ε (Figures 7a and 7b), and thus, we consider D to be negligibly small compared with the remaining three terms (P_s, P_b, and ε; McPhee, 2008a). Therefore, at this site, the TKE budget beneath Larsen C (Equation (10)) reduces to a balance between shear production, buoyancy production/loss, and dissipation (McPhee & Martinson, 1994):

$$P_s + P_b = \varepsilon. \tag{14}$$

From the observations available, we cannot evaluate the buoyancy production/loss term directly (Equation (12)). However, by writing the shear production term (Equation (11)) as a function of the observed friction velocity (Figure 7c) and mixing length (Figure 7d; McPhee, 2008a)

$$P_s = \frac{u_*^3}{\lambda_m}, \tag{15}$$

we can evaluate the balance between the rate of shear production and the rate of dissipation of TKE at both MAVS, and thus indirectly derive the importance of buoyancy beneath Larsen C from the residual.

Over the full range of ε observed at both MAVS, the rate of shear production of TKE is very similar to the rate of TKE dissipation (Figure 8). Within the individual error bars, all data points lie on, or are very close to, the one-to-one line, and the residuals are no larger than the shear production or dissipation terms themselves. Therefore, buoyancy production/loss of TKE beneath Larsen C can be no larger than the shear production of TKE for any mean flow speed.

We can further refine our estimates of the importance of P_b, however, by considering the possible sources of buoyancy in the ice shelf-ocean boundary layer. At the depths of the MAVS, the water column beneath Larsen C is predominantly homogenous, with very weak stratification (Figures 2b and 2c; Nicholls et al., 2012). Thus, the largest source of buoyancy to the boundary layer is that arising from basal melting. As the rate of basal melting at the ice shelf base is given by the divergence of the sensible heat flux at the phase change interface (Jenkins et al., 2010), the kinematic heat flux at the ice shelf-ocean boundary required to drive an observed melt rate is given by

$$\langle w' T_w' \rangle_0 = \frac{1}{\rho_w c_w}\left(\rho_i L_i \dot{m} - K_i \left.\frac{\partial T_i}{\partial z}\right|_0\right), \tag{16}$$

where T is temperature, ρ is density, c is specific heat capacity, $\dot{m}$ is basal melt rate, L is latent heat of fusion, K is thermal conductivity of ice ($K_i = \rho_i c_i \kappa_i^T$, where κ^T is thermal diffusivity), and z is depth. The subscripts i,0, and w refer to ice, ice-ocean boundary, and water, respectively. The salt flux associated with this heat flux can be broadly approximated as

$$\langle w' S_w' \rangle_0 = \frac{c_w (S_w - S_i)}{L_i} \langle w' T_w' \rangle_0, \tag{17}$$

where S is salinity (McPhee, 1992). Under Larsen C, S_w is set to 34.54 (Nicholls et al., 2012), and S_i is assumed to be zero. Finally, the rate of TKE production by the buoyancy forces associated with the observed melt rate is

$$P_b = -g\left(\beta\langle w' S_w' \rangle_0 - \alpha\langle w' T_w' \rangle_0\right), \tag{18}$$

where g is acceleratain due to gravity and α and β are the thermal expansion coefficient and saline contraction coefficient calculated at a temperature, salinity, and pressure of -2.05 °C, 34.54, and 304 dbar (Nicholls et al., 2012). From the ULS, the mean basal melt rate is 0.7 m/year, and from thermistors frozen into the ice shelf, the temperature gradient within the ice at the ice-ocean boundary is -0.11°C/m. This implies a mean kinematic heat flux of 1.7×10^{-6} K m/s, and an associated salt flux of 7.0×10^{-7} psu m/s. Together these give a stabilizing buoyancy flux of -4.9×10^{-9} W/kg.

This buoyancy flux from melting is an order of magnitude smaller than the observed rate of dissipation and shear production of TKE (Figure 8). Even for the highest rates of basal melting observed by the ULS (3.88 m/year), the maximum stabilizing buoyancy flux is -2.6×10^{-8} W/kg. This remains an order of magnitude smaller than the maximum rate of TKE dissipation and shear production. As the maximum melt rate and thus buoyancy production only occurs in conjunction with the highest rates of shear production due to tidal forcing, it is unlikely that the buoyancy production rate ever exceeds the shear production rate. Thus, we conclude that buoyancy forces are negligible at the depth of either MAVS and that the TKE budget is reduced to a balance between shear production and dissipation. Any input of freshwater from basal melting is rapidly mixed throughout the boundary layer and does not have a lasting impact on the turbulent environment. Indeed, the median Richardson number derived from the CTD profiles and the median velocity shear between the upper and lower MAVS is 0.04, with an interquartile range of 0.01 to 0.18 based on the spread in the velocity shear. A Richardson number of less than 0.25 indicates that shear instabilities can overcome stratification and drive turbulence in the water column. We consider the small residuals in excess of the error bars in Figure 8 to be largely a result of observational uncertainty.

The dominance of shear production over buoyancy production is supported by estimating the Obukhov length scale, which represents the depth below the boundary where the magnitude of the buoyancy term is equal to that of the shear production term ($\kappa = 0.41$ is the Von Kármán constant):

$$L_0 = \frac{u_*^3}{\kappa\langle w' b' \rangle_0}. \tag{19}$$

L_0 is far greater than the depth of the MAVS, ranging from 67 m to over 100 m depending on the magnitude of the buoyancy flux and friction velocity, demonstrating that the shear production term dominates over the buoyancy term.

4.2. Turbulent Length Scales

The ice shelf-ocean boundary layer can be broadly split into three distinct regions: the interfacial sublayer adjacent to the ice shelf base (mm to cm) where molecular viscosity dominates the flow, the surface layer (a few meters) where the law of the wall scaling applies and distance to the boundary is the important dynamical length scale, and the outer layer (tens of meters) where the Earth's rotation limits the turbulent length scales (Holland & Jenkins, 1999; McPhee, 2008a; Shaw et al., 2008).

In the absence of buoyancy, the surface layer is confined to the region of the boundary layer where the ratio between the measurement depth, z_m, and the Ekman boundary layer depth scale, d_E,

$$\eta = \frac{z_m}{d_E} = \frac{|f_\Omega| z_m}{u_{*0}} \tag{20}$$

is less than 0.05 (f_Ω is the Coriolis parameter. Hereinafter η is referred to as the scaled depth; Shaw et al., 2008). Work under drifting pack ice in the Arctic and the Antarctic (e.g., McPhee, 1994, 2002, 2008b) has demonstrated that in the surface layer, mixing length scales with distance from the boundary as $\kappa|z_m|$. In contrast, in the outer layer mixing length scales with the planetary depth scale as $\Lambda_* u_{*0}/|f_\Omega|$ (where Λ_* is a similarity constant equal to 0.028 and u_{*0} is the friction velocity at the ice-ocean boundary; McPhee, 1994). Thus, at any given depth in the boundary layer, the mixing length should be the smaller of $\kappa|z_m|$ or $\Lambda_* u_{*0}/|f_\Omega|$, depending on whether the measurement level is in the surface layer or the outer layer (McPhee, 2008a). As the scaled depth and the mixing length from the planetary depth scale are formulated using the friction velocity at the ice-ocean interface (u_{*0}), they are calculated at both the upper and lower MAVS by taking the observed friction velocity from the upper MAVS. Our assumption is that the friction

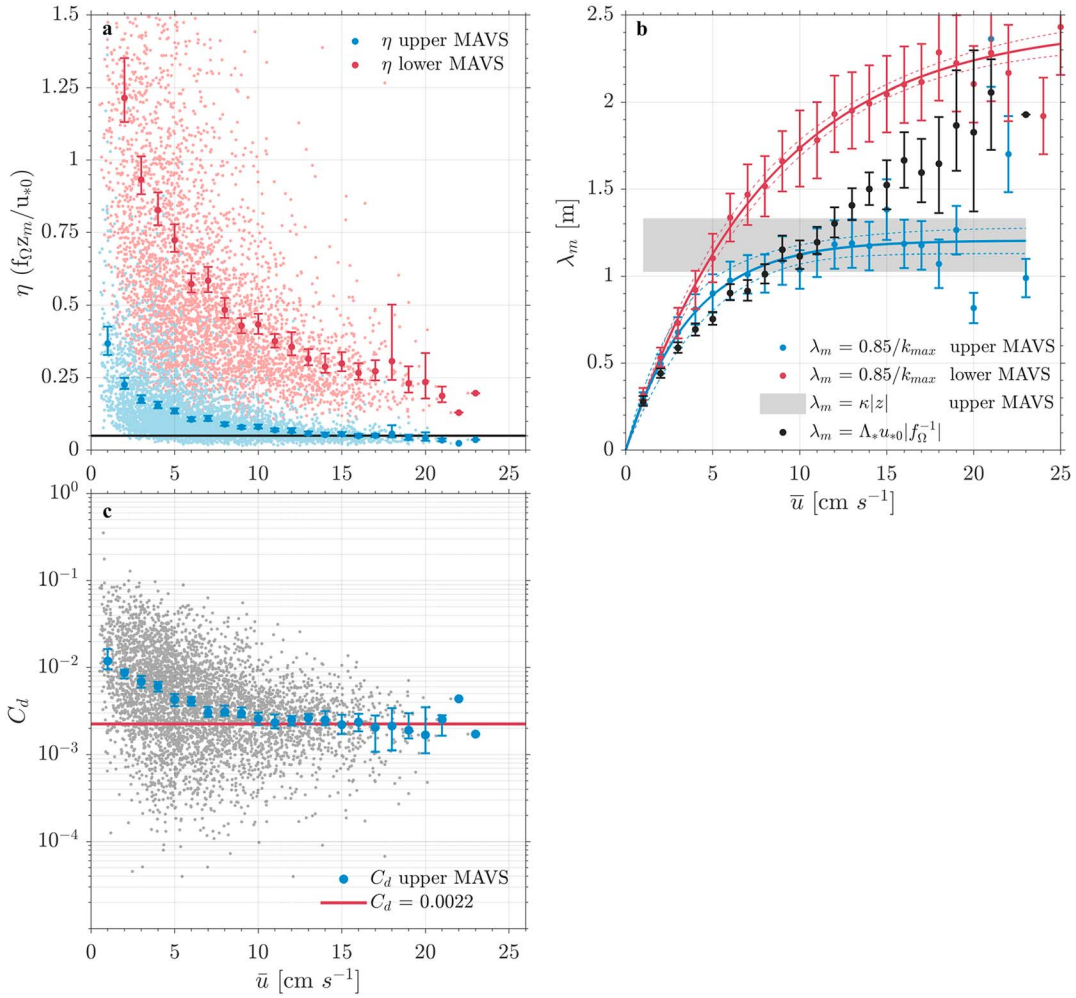

Figure 9. (a) Scaled depth as a function of mean flow speed (large colored dots) from the upper (blue) and lower (red) Modular Acoustic Velocity Sensor (MAVS). The small blue and red dots are the scaled depth from each individual MAVS burst. The black lines indicate the law of the wall cutoff. (b) Mixing length as a function of mean flow speed from the upper (blue) and lower (red) MAVS with scaling laws. The grey patch shows the range of mixing lengths expected from a law of the wall geometric scaling at the upper MAVS. The black dots show the mixing length given by the planetary depth scale calculated from the observed friction velocity at the upper MAVS (McPhee, 2008b). (c) Drag coefficient at the upper MAVS as a function of mean flow speed (large blue dots). The small grey dots show the drag coefficient from each individual MAVS burst. The red line shows the mean drag coefficients for $\overline{u} > 10$ cm/s.

velocity observed 2.5 m beneath the ice shelf base will be a more accurate estimate of the interface friction velocity than that observed 13.5 m beneath the ice shelf base.

For mean flow speeds <10 cm/s at the upper MAVS, the scaled depth is greater than 0.05 (Figure 9a) indicating that at 2.5 m beneath the ice shelf base, the upper MAVS sits in the outer region of the ice shelf-ocean boundary layer. At these mean flow speeds, mixing length increases quasi-linearly with $\overline{u}$ (blue dots Figure 9 b), and scales closely with $\lambda_m = \Lambda_* u_{*0}/|f_\Omega|$ (black dots Figure 9b). For mean flow speeds above 10 cm/s, the scaled depth, η, at the upper MAVS is close to or less than 0.05 (Figure 9a). This indicates that at 2.5 m beneath the ice shelf base, the upper MAVS is now within the surface layer/constant stress region of the ice shelf-ocean boundary layer. Mixing length is constant with mean flow speed and is set by distance from the boundary as $\lambda_m = \kappa|z_m|$ (grey patch Figure 9b). In the constant stress layer, the observed friction velocity is equal to u_{*0}.

The transition in mixing length behavior at $\overline{u} = 10$ cm/s is consistent with the behavior expected 2.5 m beneath an ice shelf (i.e., the depth of the upper MAVS) at 68°S. Here, $|f_\Omega| = 1.35 \times 10^{-4}$ s^{-1} and λ_m

should be the smaller of ~207 × u_{*0} or ~1.03 m. Thus, as we observe, λ_m should increase linearly until $u_{*0} \approx 0.5$ cm/s (i.e., $\overline{u} \approx 10$ cm/s; Figure 7c), and then remain constant for higher friction velocities (McPhee, 2008a).

Further evidence that the upper MAVS sits within the surface layer when the mean flow speed is greater than 10 cm/s comes from the scaling of the TKE dissipation rate with mean flow speed. At these flow speeds, the TKE dissipation rate is broadly proportional to $|u|^3$ (grey line in Figure 7a), which is the expected scaling for a turbulent flow in the surface layer where turbulent production and dissipation are broadly balanced (J. M. McMillan et al., 2016).

The variability in the mixing length at the upper MAVS is consistent with the thickness of the boundary layer changing in response to the magnitude of the forcing (Shaw et al., 2008). During periods of weak forcing (i.e., low mean flow speeds), we can infer that the ice shelf-ocean boundary layer is comparatively thin, and the upper MAVS sits relatively deep in the outer layer (i.e., high values of the scaled depth). In contrast, as the magnitude of the forcing increases (i.e., higher mean flow speeds), we can infer that the boundary layer thickens, and the upper MAVS sits relatively closer to, or within, the surface layer (i.e., scaled depths < 0.05).

Mixing length scaling at the lower MAVS is more complex. The scaled depth (Figure 9a) is always greater than 0.05, indicating that the lower MAVS is never within the surface layer. In this case, the maximum size of the turbulent eddies is not controlled by distance from the boundary. Indeed, at a depth of 13.5 m beneath the ice base, the surface layer mixing length of $\lambda_m = \kappa|z_m| = 5.5$ m overestimates the mixing length compared with the observed maximum of 2-2.5 m (Figure 9b). Instead, it might be expected that mixing length at the lower MAVS is controlled exclusively by rotation. This does not appear to be the case, however. The mixing length is always greater than that given by the planetary depth scale (black dots in Figure 9b), even when $\overline{u} >$ 10 cm/s and the friction velocity used to derive the planetary depth scale is equal to u_{*0}. As mixing length is known to retain its proportionality to the peak in the weighted vertical velocity wavenumber spectra at all depths in the boundary layer (McPhee & Martinson, 1994; McPhee & Smith, 1976), the difference between the observed mixing length and that given by the planetary depth scale is likely to be robust. Understanding the physical processes that control the scales of turbulence deep in the boundary layer (for example, proximity to the base of the mixed layer/mixing layer; Sutherland et al., 2014), is an important question, but it cannot be addressed with the observations available here.

4.3. Drag Coefficient and Ice Base Roughness

The drag coefficient, C_d, is a key parameter in the three-equation parameterization of ice shelf basal melting and is used to relate the free stream velocity beyond the turbulent boundary to the friction velocity at the ice shelf-ocean interface through a quadratic drag law (Jenkins et al., 2010). C_d is poorly constrained by observations, however, and is often used to tune models to match observed melt rates (e.g., Begeman et al., 2018; Dutrieux et al., 2014). In reality, the drag coefficient is likely to be highly spatially and temporally variable (Gwyther et al., 2015). Within ablation zones, C_d is likely to be small as melting tends to lead to a smoother ice interface, while in refreezing zones, C_d is likely to be larger due to the rougher nature of marine ice (Craven et al., 2009). Observationally constrained estimates of C_d for a range of different ice and boundary layer conditions is therefore an important step toward developing improved parameterizations of basal melting.

In the surface layer, the time-averaged velocity profile through the ice shelf-ocean boundary layer follows the classic logarithmic law of the wall

$$\overline{u}(z) = \frac{u_*}{\kappa} \log \frac{z}{z_0}, \tag{21}$$

where z_0 is a characteristic roughness length scale for the ice shelf base, such that $\overline{u}(z_0) = 0$. The roughness length is directly related to a neutral drag coefficient defined at any level in the log-layer through

$$C_d = \frac{u_*^2}{\overline{u}^2} = \left(\frac{1}{\kappa} \log \frac{z}{z_0}\right)^{-2}. \tag{22}$$

Thus, we can derive an observational estimate of the drag coefficient and roughness length at the upper MAVS using the average friction velocity and mean flow speed from each 14.75-min turbulent burst.

At the upper MAVS, there is substantial scatter in the drag coefficient associated with the finite length of each MAVS burst and the balance that must be struck between the desire to capture the true covariance of the turbulent eddies while avoiding longer term temporal variability. Nevertheless, when averaged as a function of mean flow speed, the drag coefficient converges toward a value of 0.0022 for flow speeds >10 cm/s (Figure 9c). This convergence is consistent with the upper MAVS sitting within the surface layer at high flow speeds, where C_d is predicted to be constant by Equation 22 (Shaw et al., 2008).

While measurements in the ice-ocean boundary layer beneath sea ice have shown that the drag coefficient can vary widely (see e.g., McPhee, 1990), the value observed here is particularly low compared with that derived from observations of basal melting beneath Ronne Ice Shelf (0.0097; Jenkins et al., 2010). Instead, it is similar to the drag coefficient observed under smooth, first-year sea ice in the Arctic (Langleben, 1982; Shirasawa & Langleben, 1976). The relatively low value of C_d is consistent with the melting conditions seen at the location of the TICs, and the likely tendency for melting to produce a smoother ice interface (Gwyther et al., 2015).

Associated with the mean drag coefficient, the roughness length scale for the ice shelf base is 0.44 mm. The roughness length is substantially smaller than that observed under sea ice in the Weddell Sea (McPhee, 2008b) and the Arctic (McPhee, 2002), likely a result of the ablation conditions eroding the roughness elements. Laboratory experiments have demonstrated that z_0 is approximately 1/30 of the vertical amplitude of the actual roughness elements. For $z_0 = 0.44$ mm, this suggests that the roughness elements (such as scallops) at the base of Larsen C ice shelf have a vertical extent of 1.3 cm.

The upstream distance affecting turbulence at a given depth in the ice shelf-ocean boundary layer can be roughly estimated through the ratio $\overline{u}/u_*$ (Morison & McPhee, 2001). For mean flow speeds above 10 cm/s at the upper MAVS, the average ratio is ~23. Consequently, the horizontal extent over which the roughness length estimated above is valid is ~60 m. It is possible that larger roughness elements may be present further upstream of this distance, and their impact on the turbulence would be observed relatively deeper in the boundary layer (McPhee, 2008b). However, as the Reynolds stress (viz. friction velocity) decreases with depth (Figure 7c), there is little evidence to suggest that the turbulence is influenced by the presence of larger roughness elements upstream of the TICs. Thus, the ice shelf base at this location appears to be smooth over wide area.

4.4. Three-Equation Melt Rate Parameterization

Our observations have shown that the cold, tidally forced boundary layer beneath Larsen C is characterized by a balance between the rate of shear production and dissipation of TKE, with little role played by buoyancy. To assess the performance of the canonical three-equation melt rate parameterization in these conditions, we compare the mean melt rate from the ULS with the mean parameterized melt rate derived from the time series of burst averaged horizontal flow speed (Figure 4a) and temperature (not shown) from the upper MAVS. Following the approach of Jenkins et al. (2010), the temperature at the MAVS derived from the Rockland MicroSquid temperature sensor is calibrated against the CTD casts taken at the time of deployment in order to remove the uncertain response of the fast-response thermistor to pressure. We estimate an uncertainty in temperature of 0.1°C.

In the three-equation parameterization, the vertical fluxes of heat and salt that control the rate of basal melting take the form of

$$C_d^{1/2}\Gamma_T\overline{u}(T_w - T_0) \text{ and } C_d^{1/2}\Gamma_S\overline{u}(S_w - S_0), \tag{23}$$

where Γ_T and Γ_S are dimensionless turbulent transfer coefficients for heat and salt, and $(T_w - T_0)$ and $(S_w - S_0)$ are the difference between the far field and ice-ocean interface temperature and salinity, respectively (Jenkins et al., 2010). The far field salinity is not observed, so it is fixed at a value of 34.54 (Nicholls et al., 2012), and the far field temperature is taken from the upper MAVS. Ideally, the value of Γ_T and Γ_S should be derived directly from the turbulent heat and salt flux; however, this is not possible with the observations we have available. Instead, to derive the value of Γ_T and Γ_S, we take the product $C_d^{1/2}\Gamma_T$ as 0.0011 (which is the parameter most directly constrained by observations; Jenkins et al., 2010) and combine it with our observed drag coefficient of 0.0022 (Figure 9c). This gives a heat transfer coefficient of $\Gamma_T = 0.0235$, and a salt transfer coefficient of $\Gamma_s = 6.7\times10^{-4}$ (assuming the ratio $\Gamma_T/\Gamma_s = 35$). Given these parameters and the

uncertainty in the temperature and salinity, the mean (± one standard deviation) parameterized melt rate is 0.69 ± 0.6 m/year. This compares very favorably with the mean melt rate of 0.70 ± 1.0 m/year observed by the ULS.

In spite of this agreement, our observations highlight a structural deficit in the three-equation parameterization. As currently formulated, the three-equation parameterization describes the friction velocity at the ice shelf-ocean interface as a function of the drag coefficient and the mean flow speed: $u_* = \sqrt{C_d}\overline{u}$ (Figure 7c; Jenkins et al., 2010). This functional form of the friction velocity requires the law of the wall scaling to hold (Equation (22)), and thus is only valid in the log-layer region of the ice shelf-ocean boundary layer. As we have seen in section 4.2, however, the log-layer can be less than 2.5 m thick for $\overline{u} < 10$ cm/s, and thus at these low flow speeds $u_* = \sqrt{C_d}\overline{u}$ substantially underestimates the friction velocity (Figure 7c). As the ice shelf-ocean boundary layer beneath Larsen C is dominated by strong tidal currents, the impact of this structural deficit on the parameterized melt rate is small. However, when using the three-equation parameterization in conjunction with observations collected outside of the log-layer in more quiescent ice shelf-ocean boundary layers, or in z-coordinate models where the upper grid cell beneath the ice shelf base can be tens of meters thick (e.g., Losch, 2008), the impact on the parameterized melt rate could be much larger. Indeed, with a fixed far field temperature and salinity of -2.08°C and 34.54, respectively, and the same turbulent transfer coefficients as those discussed above, the percentage difference in the parameterized melt rate introduced by using $u_* = \sqrt{C_d}\overline{u}$ when the law of the wall is not valid increases from 24% at $\overline{u} = 9$ cm/s to 68% at $\overline{u} = 1$ cm/s. Addressing this issue in the three-equation parameterization would be a worthwhile endeavor.

Notwithstanding the structural deficit discussed above, our results demonstrate that the canonical three-equation parameterization of Jenkins et al. (2010) can perform well in cold, tidally forced boundary layers where background flow speeds are high, stratification is unimportant, and the ice base is smooth. In addition, while $C_d^{1/2}\Gamma_T = 0.0011$ was derived by matching scalar fluxes beneath Ronne Ice Shelf, our analysis further demonstrates that its value is robust for a different cold-cavity ice shelf. As $C_d^{1/2}\Gamma_T$ is the controlling parameter, the mean melt rate calculated by taking the drag coefficient of 0.0097 ($\Gamma_T = 0.011$ and $\Gamma_s = 3.1\times10^{-4}$) directly from Jenkins et al. (2010) is identical to that derived above. As cautioned by Jenkins et al., however, that drag coefficient is derived from scalar rather than momentum fluxes and should be used with care. Instead, as the drag coefficient is also an important term in the momentum formulations used in many numerical models, when modeling cold cavity ice shelf-ocean boundary layers that are characterized by smooth ice, weak stratification and high flow speeds, we encourage the use of a drag coefficient closer to our momentum-flux derived estimate of 0.0022 and $C_d^{1/2}\Gamma_T = 0.0011$ to derive matching heat and salt transfer coefficients.

5. Conclusions

We have presented a yearlong observational time series of the turbulent environment in a cold, tidally forced boundary layer beneath an Antarctic ice shelf. Our results show that the rate of TKE dissipation ranges from ~10^{-9} to ~10^{-6} W/kg as a function of mean flow speed and that the TKE budget 2.5 and 13.5 m beneath the ice shelf base is characterized by a balance between shear production and dissipation. Buoyancy effects appear to be negligible, and the input of freshwater from basal melting appears to play little role in the TKE budget. While buoyancy forces are known to be important elsewhere (e.g., beneath George VI Ice Shelf or Pine Island Ice Shelf; Kimura et al., 2015, 2016; Stanton et al., 2013), these locations are characterized by substantially weaker tidal forcing and lower shear production rates of TKE. Therefore, we propose that strong tidal forcing is a key factor in generating the shear-dominated regime such as that we have observed beneath Larsen C Ice Shelf. In other tidally dominated sub-ice shelf cavities, such as that beneath Filchner-Ronne Ice Shelf, we would expect the same behavior observed here to broadly hold, and for the TKE budget to be characterized by a balance between the TKE dissipation rate and shear production.

We infer from our observations that the ice shelf-ocean boundary layer thickens with higher mean flow speeds, and for flow speeds above 10 cm/s, scaling arguments suggest that the TIC deployed 2.5 m beneath the ice shelf base is within the logarithmic layer. The drag coefficient derived from observations at these high

mean flow speeds is 0.0022, and the roughness length is 0.44 mm. This suggests that the ice shelf base is smooth, consistent with the ablation conditions that are observed.

The melt rate predicted by the canonical three-equation melt rate parameterization agrees with the observed melt rate from an ULS, suggesting that the parameterization can perform well for smooth ice in homogenous and tidally forced boundary layers found beneath cold cavity ice shelves. This result is mirrored by the recent large eddy simulations of the ice shelf-ocean boundary layer by Vreugdenhil and Taylor (2019). Their results also show that when stratification is weak and the boundary layer is fully turbulent, melt rates predicted by the three-equation parameterization compare very well with those derived directly from the large eddy simulations. The key parameter appears to be the product $C_d^{1/2}\Gamma_T$, with this study, as well as Jenkins et al. (2010) and Vreugdenhil and Taylor (2019), suggesting that it should take a value of 0.011.

Notwithstanding the good agreement seen between the parameterized and observed melt rate under Larsen C, our results also highlight a structural deficit in the three-equation parameterization associated with the law of the wall assumption used to relate the mean flow speed to the friction velocity at the ice-ocean interface through the drag coefficient (Jenkins et al., 2010). At low flow speeds, the upper MAVS is outside of the log-layer and the law of the wall assumption underestimates the friction velocity (Figure 7c). While the high flow speeds beneath Larsen C limit the impact of this structural deficit on the parameterized melt rate, if the three-equation parameterization is used in conjunction with observations taken outside of the log-layer in more quiescent boundary layers, or in z-coordinate numerical models where the upper grid cell can be tens of meters thick, the effect is likely to be much larger.

Looking to the future, much work remains to be done in improving the formulations of basal melting in numerical models. Alongside addressing the structural deficit discussed above, it is known that three-equation parameterization does not hold for all boundary layer types (e.g., Kimura et al., 2015; McConnochie & Kerr, 2017), and subsequent studies should aim at assessing and understanding the relevant processes in these more complex turbulent environments. Furthermore, the technical challenges involved in measuring the scalar fluxes beneath Antarctic ice shelves (especially the salt flux) must be overcome to estimate, for example, the turbulent heat and salt turbulent transfer coefficients directly (i.e., Γ_T and Γ_S; Jenkins et al., 2010). Observations of this type will greatly improve our ability to derive and incorporate accurate parameterizations of basal melting in global climate models, allowing us to reduce the uncertainty in estimates of the future contribution of the Antarctic Ice Sheet to global sea level rise.

Appendix A: Noise Floor and Filtering

The combination of the small sensor geometry and the differential travel time technique employed by the MAVS makes it a highly accurate velocity instrument, with a stated velocity accuracy of 0.5 mm/s. To determine the actual noise level of the velocity measurements, however, the turbulent velocity frequency spectra from each MAVS burst were bin averaged according to the mean flow speed (Figure A1). At low flow speeds (1 to 3 cm/s) and near the Nyquist frequency (f_N=2.5 Hz), the spectra level out and approach the noise floor as white noise begins to dominate. Integrating the noise floor (Φ_n; black dashed lines in Figure A1) over the frequency domain for each velocity component (Peterson et al., 2017)

$$\sigma_n = \int_0^{f_N} \Phi_n df, \tag{A1}$$

$$u_n = \sqrt{\sigma_n}, \tag{A2}$$

gives a mean noise level of $[u_n, v_n] = 0.6$ mm/s, and $w_n = 0.3$ mm/s, in very good agreement with the stated accuracy.

Peaks in the turbulent velocity spectra are generally indicative of extraneous sources of noise contaminating the turbulent velocity fluctuations (McPhee, 2008a). At higher mean flow speeds (>3 cm/s), a peak appears in the frequency spectra close to the Nyquist frequency, and the spectra remain elevated above the noise floor. This peak is associated with vortex shedding off the central strut of the MAVS (Trivett et al., 1990). The frequency of vortex shedding

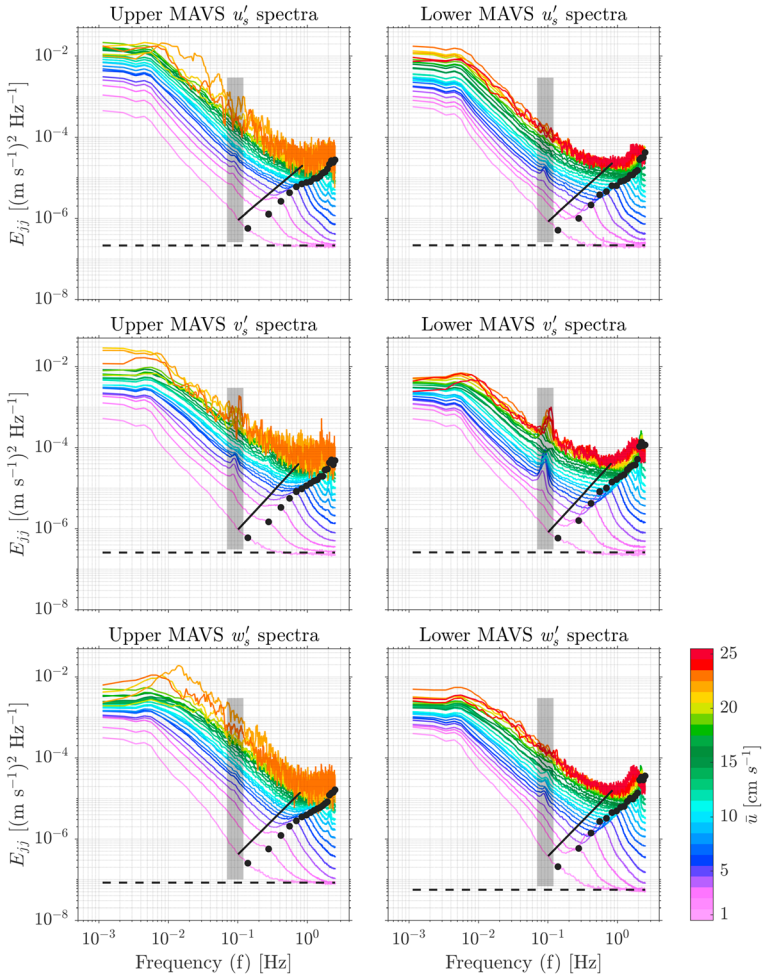

Figure A1. Turbulent velocity frequency spectra for the along- and cross-stream velocity components at the upper and lower Modular Acoustic Velocity Sensor (MAVS) as a function of mean flow speed. The black dashed line indicates the noise floor, E_{jj}^n, for each velocity component, while the black dot indicates the frequency of vortex shedding off the central MAVS strut as a function of mean flow speed. The solid black line marks the low-pass filter frequency cutoff designed to minimize the effect of vortex shedding on the covariance estimates, whilst the grey patch marks the frequency range that is band-pass filtered in order to minimize the effect of cable strumming on the covariance estimates.

$$f_s = \frac{\overline{u}St}{D}, \tag{A3}$$

increases with mean flow speed (black dots in Figure A1), where $St = 0.18$ is the Strouhal number and D is the diameter of the central strut (13 mm). As the shedding frequency approaches and then exceeds the Nyquist frequency (mean flow speeds >17 cm/s), unresolved, high-frequency variability is increasingly aliased by the MAVS, elevating the spectra above the noise floor.

A second peak exists in the frequency spectra at a frequency of approximately 0.1 Hz. The frequency of the peak is invariant with flow speed, and the peak is predominantly present in the horizontal cross-stream velocity component (v). We attribute this peak to strumming of the flexible mooring cable in the cross-flow direction (McPhee, 2008a).

While the absolute energy level of these different noise sources is relatively weak compared with the energy level at lower frequencies, the noise is highly correlated between the different velocity components. As a result, the noise severely contaminates the covariance estimates $\langle u_s' w_s' \rangle$ and $\langle v_s' w_s' \rangle$ and hence the friction velocity (u_*). To counteract this noise, a low-pass filter with a cutoff frequency that increases with mean flow speed (black line in Figure A1) is used to minimize the effect of vortex shedding, and a band-pass filter

between 0.08 and 0.11 Hz is used to minimize the effect of cable strumming (grey patch in Figure A1). By applying these filters, the magnitude of the friction velocity is reduced on average by 15%, but the reduction can be up to 30% for high mean flow speeds at the lower MAVS.

The noise level for u_* itself is estimated from synthetic time series of u, v, and w with variance equal to the noise floor (σ_n in equation (A1); Peterson et al., 2017). Using 1,000 realizations of the synthetic velocity time series, the mean noise floor $u_{*n} = 6 \times 10^{-3}$ cm/s.

Acknowledgments
We are grateful for the comments from Satoshi Kimura and Carolyn Begeman that significantly improved the manuscript. The work in this paper is part of the Sub Ice Shelf Boundary Layer Experiment, funded by the UK Natural Environment Research Council (NERC) grant NE/H009205/1. P. D. and K. N. also received funding from the NERC Ice shelves in a warming world: Filchner Ice Shelf system program (grant NE/L013770/1). The turbulence data are available from the UK Polar Data Centre (https://doi.org/10.5285/16ee2665-d0d0-41b9-a046-23b0a7369c61)

References

Arthern, R. J., & Williams, C. R. (2017). The sensitivity of West Antarctica to the submarine melting feedback. *Geophysical Research Letters*, *44*, 2352–2359. https://doi.org/10.1002/2017GL072514

Assmann, K. M., Darelius, E., Wåhlin, A. K., Kim, T. W., & Lee, S. H. (2019). Warm circumpolar deep water at the Western Getz Ice Shelf Front, Antarctica. *Geophysical Research Letters*, *46*(2), 870–878. https://doi.org/10.1029/2018GL081354

Bamber, J. L., Riva, R. E. M., Vermeersen, B. L. A., & LeBrocq, A. M. (2009). Reassessment of the potential sea-level rise from a collapse of the West Antarctic Ice Sheet. *Science*, *324*, 901–903. https://doi.org/10.1126/science.1169335

Batchelor, G. K. (1976). *The Theory of Homogeneous Turbulence*. Cambridge, UK: Cambridge University Press.

Begeman, C. B., Tulaczyk, S. M., Marsh, O. J., Mikucki, J. A., Stanton, T. P., Hodson, T. O., et al. (2018). Ocean stratification and low melt rates at the Ross Ice Shelf Grounding Zone. *Journal of Geophysical Research: Oceans*, *123*, 7438–7452. https://doi.org/10.1029/2018JC013987

Biltoft, C. A. (2001). Some thoughts on local isotropy and the 4/3 lateral to longitudinal velocity spectrum ratio. *Boundary-Layer Meteorology*, *100*, 393–404. https://doi.org/10.1023/A:1019289915930

Bluteau, C. E., Jones, N. L., & Ivey, G. N. (2011). Estimating turbulent kinetic energy dissipation using the inertial subrange method in environmental flows. *Limnology and Oceanography: Methods*, *9*, 302–321. https://doi.org/10.4319/lom.2011.9.302

Chamecki, M., & Dias, N. L. (2004). The local isotropy hypothesis and the turbulent kinetic energy dissipation rate in the atmospheric surface layer. *Quarterly Journal of the Royal Meteorological Society*, *130*, 2733–2752. https://doi.org/10.1256/qj.03.155

Church, J. A., Clark, P. U., Cazenave, A., Gregory, J. M., Jevrejeva, S., Levermann, A., et al. (2013). Sea Level Change. In T. F. Stocker, D. Qin, G.-K. Plattner, M. Tignor, S. K. Allen, J. Boschung, et al. (Eds.), *Climate change 2013—The physical science basis*, (pp. 1137–1216). Cambridge, United Kingdom and New York, NY, USA: Cambridge University Press. https://doi.org/10.1017/CBO9781107415324.026

Codiga, D. L. (2011). *Unified tidal analysis and prediction using the UTide Matlab functions*. URI/GSO Technical Report 2011-01, Narragansett, RI: University of Rhode Island. https://doi.org/10.13140/RG.2.1.3761.2008

Cornford, S. L., Martin, D. F., Payne, A. J., Ng, E. G., Le Brocq, A. M., Gladstone, R. M., et al. (2015). Century-scale simulations of the response of the West Antarctic Ice Sheet to a warming climate. *The Cryosphere*, *9*, 1579–1600. https://doi.org/10.5194/tc-9-1579-2015

Craven, M., Allison, I., Fricker, H. A., & Warner, R. (2009). Properties of a marine ice layer under the Amery Ice Shelf, East Antarctica. *Journal of Glaciology*, *55*(192), 717–728. https://doi.org/10.3189/002214309789470941

Dansereau, V., Heimbach, P., & Losch, M. (2014). Simulation of subice shelf melt rates in a general circulation model: Velocity-dependent transfer and the role of friction. *Journal of Geophysical Research: Oceans*, *119*, 1765–1790. https://doi.org/10.1002/2013JC008846

Davis, P. E. D., & Nicholls, K. W. (2019). *Turbulence beneath Larsen C ice shelf, Antarctica*. United Kingdom: UK Polar Data Centre, Natural Environment Research Council, UK Research & Innovation. https://doi.org/10.5285/16ee2665-d0d0-41b9-a046-23b0a7369c61

DeConto, R. M., & Pollard, D. (2016). Contribution of Antarctica to past and future sea-level rise. *Nature*, *531*, 591–597. https://doi.org/10.1038/nature17145

Dutrieux, P., De Rydt, J., Jenkins, A., Holland, P. R., Ha, H. K., Lee, S. H., et al. (2014). Strong sensitivity of Pine Island ice-shelf melting to climatic variability. *Science*, *343*, 174–178. https://doi.org/10.1126/science.1244341

Favier, L., Durand, G., Cornford, S. L., Gudmundsson, G. H., Gagliardini, O., Gillet-Chaulet, F., et al. (2014). Retreat of Pine Island Glacier controlled by marine ice-sheet instability. *Nature Climate Change*, *4*, 117–121. https://doi.org/10.1038/nclimate2094

Foldvik, A., Gammelsrød, T., Østerhus, S., Fahrbach, E., Rohardt, G., Schröder, M., et al. (2004). Ice shelf water overflow and bottom water formation in the southern Weddell Sea. *Journal of Geophysical Research*, *109*, C02015. https://doi.org/10.1029/2003JC002008

Foldvik, A., Gammelsrød, T., & Tørresen, T. (1985). Circulation and water masses on the southern Weddell Sea shelf. In S. S. Jacobs (Ed.), *Oceanology of the Antarctic Continental Shelf*, *Antarctic Research Series*, (Vol. 43, pp. 5–20). Washington D.C., USA: American Geophysical Union. https://doi.org/10.1029/AR043p0005

Fretwell, P., Pritchard, H. D., Vaughan, D. G., Bamber, J. L., Barrand, N. E., Bell, R., et al. (2013). Bedmap2: Improved ice bed, surface and thickness datasets for Antarctica. *The Cryosphere*, *7*, 375–393. https://doi.org/10.5194/tc-7-375-2013

Fürst, J. J., Durand, G., Gillet-Chaulet, F., Tavard, L., Rankl, M., Braun, M., & Gagliardini, O. (2016). The safety band of Antarctic ice shelves. *Nature Climate Change*, *6*, 479–482. https://doi.org/10.1038/nclimate2912

Goldberg, D. N., Gourmelen, N., Kimura, S., Millan, R., & Snow, K. (2019). How accurately should we model ice shelf melt rates? *Geophysical Research Letters*, *46*, 189–199. https://doi.org/10.1029/2018GL080383

Gwyther, D. E., Galton-Fenzi, B. K., Dinniman, M. S., Roberts, J. L., & Hunter, J. R. (2015). The effect of basal friction on melting and freezing in ice shelf–ocean models. *Ocean Modelling*, *95*, 38–52. https://doi.org/10.1016/j.ocemod.2015.09.004

Hellmer, H. H., Kauker, F., Timmermann, R., Determann, J., & Rae, J. (2012). Twenty-first-century warming of a large Antarctic ice-shelf cavity by a redirected coastal current. *Nature*, *485*, 225–228. https://doi.org/10.1038/nature11064

Hellmer, H. H., Kauker, F., Timmermann, R., & Hattermann, T. (2017). The fate of the Southern Weddell Sea Continental Shelf in a warming climate. *Journal of Climate*, *30*, 4337–4350. https://doi.org/10.1175/JCLI-D-16-0420.1

Holland, D. M., & Jenkins, A. (1999). Modeling thermodynamic ice–ocean interactions at the base of an Ice Shelf. *Journal of Physical Oceanography*, *29*, 1787–1800. https://doi.org/10.1175/1520-0485(1999)029<1787:MTIOIA>2.0.CO;2

IMBIE (2018). Mass balance of the Antarctic Ice Sheet from 1992 to 2017. *Nature*, *558*(7709), 219–222. https://doi.org/10.1038/s41586-018-0179-y

Jacobs, S. S., Jenkins, A., Giulivi, C. F., & Dutrieux, P. (2011). Stronger ocean circulation and increased melting under Pine Island Glacier ice shelf. *Nature Geoscience: Oceans*, *4*, 519–523. https://doi.org/10.1038/ngeo1188

Jenkins, A. (1999). The impact of melting ice on ocean waters. *Journal of Physical Oceanography*, *29*, 2370–2381. https://doi.org/10.1175/1520-0485(1999)029<2370:TIOMIO>2.0.CO;2

Jenkins, A., Dutrieux, P., Jacobs, S., Steig, E., Gudmundsson, H., Smith, J., & Heywood, K. (2016). Decadal ocean forcing and Antarctic ice sheet response: Lessons from the Amundsen Sea. *Oceanography*, *29*, 106–117. https://doi.org/10.5670/oceanog.2016.103

Jenkins, A., Nicholls, K. W., & Corr, H. F. J. (2010). Observation and parameterization of ablation at the base of Ronne Ice Shelf, Antarctica. *Journal of Physical Oceanography*, *40*, 2298–2312. https://doi.org/10.1175/2010JPO4317.1

Joughin, I., Smith, B. E., & Medley, B. (2014). Marine ice sheet collapse potentially under way for the Thwaites Glacier Basin, West Antarctica. *Science*, *344*, 735–738. https://doi.org/10.1126/science.1249055

Khazendar, A., Rignot, E., Schroeder, D. M., Seroussi, H., Schodlok, M. P., Scheuchl, B., et al. (2016). Rapid submarine ice melting in the grounding zones of ice shelves in West Antarctica. *Nature Communications*, *7*, 13243. https://doi.org/10.1038/ncomms13243

Kimura, S., Jenkins, A., Dutrieux, P., Forryan, A., Naveira Garabato, A. C., & Firing, Y. (2016). Ocean mixing beneath Pine Island Glacier ice shelf, West Antarctica. *Journal of Geophysical Research: Oceans*, *121*, 8496–8510. https://doi.org/10.1002/2016JC012149

Kimura, S., Nicholls, K. W., & Venables, E. (2015). Estimation of ice shelf melt rate in the presence of a thermohaline staircase. *Journal of Physical Oceanography*, *45*, 133–148. https://doi.org/10.1175/JPO-D-14-0106.1

Langleben, M. P. (1982). Water drag coefficient of first-year sea ice. *Journal of Geophysical Research*, *87*, 573–578. https://doi.org/10.1029/JC087iC01p00573

Losch, M. (2008). Modeling ice shelf cavities in a z coordinate ocean general circulation model. *Journal of Geophysical Research*, *113*, C08043. https://doi.org/10.1029/2007JC004368

Makinson, K., Schroder, M., & Osterhus, S. (2006). Effect of critical latitude and seasonal stratification on tidal current profiles along Ronne Ice Front, Antarctica. *Journal of Geophysical Research*, *111*(C03022), 1–15. https://doi.org/10.1029/2005JC003062

McConnochie, C. D., & Kerr, R. C. (2017). Testing a common ice-ocean parameterization with laboratory experiments. *Journal of Geophysical Research: Oceans*, *122*, 5905–5915. https://doi.org/10.1002/2017JC012918

McMillan, J. M., Hay, A. E., Lueck, R. G., & Wolk, F. (2016). Rates of dissipation of turbulent kinetic energy in a high Reynolds number tidal channel. *Journal of Atmospheric and Oceanic Technology*, *33*, 817–837. https://doi.org/10.1175/JTECH-D-15-0167.1

McMillan, M., Shepherd, A., Sundal, A., Briggs, K., Muir, A., Ridout, A., et al. (2014). Increased ice losses from Antarctica detected by CryoSat-2. *Geophysical Research Letters*, *41*, 3899–3905. https://doi.org/10.1002/2014GL060111

McPhee, M. G. (1990). Small-scale processes. In *Polar Oceanography. Part A Physical Science*, (pp. 287–334). Elsevier. https://doi.org/10.1016/B978-0-12-653031-5.50011-4

McPhee, M. G. (1992). Turbulent heat flux in the upper ocean under sea ice. *Journal of Geophysical Research*, *97*, 5,365–5,379. https://doi.org/10.1029/92JC00239

McPhee, M. G. (1994). On the turbulent mixing length in the oceanic boundary layer. *Journal of Physical Oceanography*, *24*, 2014–2031. https://doi.org/10.1175/1520-0485(1994)024<2014:OTTMLI>2.0.CO;2

McPhee, M. G. (2002). Turbulent stress at the ice/ocean interface and bottom surface hydraulic roughness during the SHEBA drift. *Journal of Geophysical Research*, *107*, 8037. https://doi.org/10.1029/2000JC000633

McPhee, M. G. (2004). A spectral technique for estimating turbulent stress, scalar flux magnitude, and eddy viscosity in the ocean boundary layer under pack ice. *Journal of Physical Oceanography*, *34*, 2180–2188. https://doi.org/10.1175/1520-0485(2004)034<2180:ASTFET>2.0.CO;2

Mcphee, M. G. (2008a). *Air-ice-ocean interaction: Turbulent ocean boundary layer exchange processes*. New York, NY: Springer New York. https://doi.org/10.1007/978-0-387-78335-2

McPhee, M. G. (2008b). Physics of early summer ice/ocean exchanges in the western Weddell Sea during ISPOL. *Deep sea research. Part II: Topical studies in oceanography*, *55*, 1075–1097. https://doi.org/10.1016/j.dsr2.2007.12.022

McPhee, M. G., & Martinson, D. G. (1994). Turbulent mixing under drifting pack ice in the Weddell Sea. *Science*, *263*, 218–221. https://doi.org/10.1126/science.263.5144.218

McPhee, M. G., Morison, J. H., & Nilsen, F. (2008). Revisiting heat and salt exchange at the ice-ocean interface: Ocean flux and modeling considerations. *Journal of Geophysical Research*, *113*, C06014. https://doi.org/10.1029/2007JC004383

McPhee, M. G., & Smith, J. D. (1976). Measurements of the turbulent boundary layer under pack ice. *Journal of Physical Oceanography*, *6*, 696–711. https://doi.org/10.1175/1520-0485(1976)006<0696:MOTTBL>2.0.CO;2

Milillo, P., Rignot, E., Rizzoli, P., Scheuchl, B., Mouginot, J., Bueso-Bello, J., & Prats-Iraola, P. (2019). Heterogeneous retreat and ice melt of Thwaites Glacier, West Antarctica. *Science Advances*, 5. https://doi.org/10.1126/sciadv.aau3433

Morison, J. H., & McPhee, M. (2001). Ice-ocean interaction. In J. Steele, S. Thorpe, & K. Turekian (Eds.), *Encyclopedia of Ocean Sciences*, (2nd ed.pp. 1271–1281). New York: Academic Press. https://doi.org/10.1006/rwos.2001.0003

Mouginot, J., Rignot, E., & Scheuchl, B. (2014). Sustained increase in ice discharge from the Amundsen Sea Embayment, West Antarctica, from 1973 to 2013. *Geophysical Research Letters*, *41*, 1576–1584. https://doi.org/10.1002/2013GL059069

Nicholls, K. W., Makinson, K., & Venables, E. J. (2012). Ocean circulation beneath Larsen C ice shelf, Antarctica from in situ observations. *Geophysical Research Letters*, *39*, L19608. https://doi.org/10.1029/2012GL053187

Paolo, F. S., Fricker, H. A., & Padman, L. (2015). Volume loss from Antarctic ice shelves is accelerating. *Science*, *348*, 327–331. https://doi.org/10.1126/science.aaa0940

Park, J. W., Gourmelen, N., Shepherd, A., Kim, S. W., Vaughan, D. G., & Wingham, D. J. (2013). Sustained retreat of the Pine Island Glacier. *Geophysical Research Letters*, *40*, 2137–2142. https://doi.org/10.1002/grl.50379

Peterson, A. K., Fer, I., McPhee, M. G., & Randelhoff, A. (2017). Turbulent heat and momentum fluxes in the upper ocean under Arctic sea ice. *Journal of Geophysical Research: Oceans*, *122*, 1439–1456. https://doi.org/10.1002/2016JC012283

Pope, S. B. (2000). *Turbulent Flows*. Cambridge, UK: Cambridge University Press. https://doi.org/10.1017/CBO9780511840531

Prandle, D. (1982). The vertical structure of tidal currents. *Geophysical and Astrophysical Fluid Dynamics*, *22*, 29–49.

Pritchard, H. D., Ligtenberg, S. R. M., Fricker, H. A., Vaughan, D. G., van den Broeke, M. R., & Padman, L. (2012). Antarctic ice-sheet loss driven by basal melting of ice shelves. *Nature*, *484*, 502–505. https://doi.org/10.1038/nature10968

Reese, R., Gudmundsson, G. H., Levermann, A., & Winkelmann, R. (2018). The far reach of ice-shelf thinning in Antarctica. *Nature Climate Change*, *8*, 53–57. https://doi.org/10.1038/s41558-017-0020-x

Rignot, E., Mouginot, J., Morlighem, M., Seroussi, H., & Scheuchl, B. (2014). Widespread, rapid grounding line retreat of Pine Island, Thwaites, Smith, and Kohler glaciers, West Antarctica, from 1992 to 2011. *Geophysical Research Letters*, *41*, 3502–3509. https://doi.org/10.1002/2014GL060140

Rignot, E., Mouginot, J., Scheuchl, B., van den Broeke, M., van Wessem, M. J., & Morlighem, M. (2019). Four decades of Antarctic Ice Sheet mass balance from 1979–2017. *Proceedings of the National Academy of Sciences*, *116*, 1095–1103. https://doi.org/10.1073/pnas.1812883116

Scheuchl, B., Mouginot, J., Rignot, E., Morlighem, M., & Khazendar, A. (2016). Grounding line retreat of Pope, Smith, and Kohler Glaciers, West Antarctica, measured with Sentinel-1a radar interferometry data. *Geophysical Research Letters*, *43*, 8572–8579. https://doi.org/10.1002/2016GL069287

Shaw, W. J., Stanton, T. P., McPhee, M. G., & Kikuchi, T. (2008). Estimates of surface roughness length in heterogeneous under-ice boundary layers. *Journal of Geophysical Research*, *113*, C08030. https://doi.org/10.1029/2007JC004550

Shepherd, A., Fricker, H. A., & Farrell, S. L. (2018). Trends and connections across the Antarctic cryosphere. *Nature*, *558*, 223–232. https://doi.org/10.1038/s41586-018-0171-6

Shepherd, A., Ivins, E. R., Geruo, A., Barletta, V. R., Bentley, M. J., Bettadpur, S., et al. (2012). A reconciled estimate of ice-sheet mass balance. *Science*, *338*, 1183–1189. https://doi.org/10.1126/science.1228102

Shepherd, A., Wingham, D., & Rignot, E. (2004). Warm ocean is eroding West Antarctic Ice Sheet. *Geophysical Research Letters*, *31*, L23402. https://doi.org/10.1029/2004GL021106

Shepherd, A., Wingham, D. J., & Mansley, J. A. D. (2002). Inland thinning of the Amundsen Sea sector, West Antarctica. *Geophysical Research Letters*, *29*(10), 1364. https://doi.org/10.1029/2001GL014183

Shepherd, A., Wingham, D. J., Mansley, J. A. D., & Corr, H. F. J. (2001). Inland thinning of Pine Island Glacier, West Antarctica. *Science*, *291*, 862–864. https://doi.org/10.1126/science.291.5505.862

Shirasawa, K., & Langleben, M. P. (1976). Water drag on arctic sea ice. *Journal of Geophysical Research*, *81*, 6451–6454. https://doi.org/10.1029/JC081i036p06451

Smith, J. A., Andersen, T. J., Shortt, M., Gaffney, A. M., Truffer, M., Stanton, T. P., et al. (2017). Sub-ice-shelf sediments record history of twentieth-century retreat of Pine Island Glacier. *Nature*, *541*, 77–80. https://doi.org/10.1038/nature20136

Stanton, T. P., Shaw, W. J., Truffer, M., Corr, H. F. J., Peters, L. E., Riverman, K. L., et al. (2013). Channelized ice melting in the ocean boundary layer beneath Pine Island Glacier, Antarctica. *Science*, *341*, 1236–1239. https://doi.org/10.1126/science.1239373

Sutherland, G., Reverdin, G., Marié, L., & Ward, B. (2014). Mixed and mixing layer depths in the ocean surface boundary layer under conditions of diurnal stratification. *Geophysical Research Letters*, *41*, 8469–8476. https://doi.org/10.1002/2014GL061939

Tennekes, H., & Lumley, J. L. (1972). *A first course in turbulence*. Cambridge, Ma, USA: The Mit Press.

Thomson, D. J. (1982). Spectrum estimation and harmonic analysis. *Proceedings of the IEEE*, *70*, 1055–1096. https://doi.org/10.1109/PROC.1982.12433

Timmermann, R., & Hellmer, H. H. (2013). Southern Ocean warming and increased ice shelf basal melting in the twenty-first and twenty-second centuries based on coupled ice-ocean finite-element modelling. *Ocean Dynamics*, *63*, 1011–1026. https://doi.org/10.1007/s10236-013-0642-0

Trivett, D. A., Williams, A. J., & Terray, E. A. (1990). Modular acoustic velocity sensor: A general-purpose flow meter. In Proceedings of the IEEE Fourth Working Conference on Current Measurement (pp. 80–89). https://doi.org/10.1109/CURM.1990.110894

Venables, E., Nicholls, K., Wolk, F., Makinson, K., & Anker, P. (2014). Measuring turbulent dissipation rates beneath an Antarctic Ice Shelf. *Marine Technology Society Journal*, *48*, 18–24. https://doi.org/10.4031/MTSJ.48.5.8

Vreugdenhil, C. A., & Taylor, J. R. (2019). Stratification effects in the turbulent boundary layer beneath a melting ice shelf: Insights from resolved large-eddy simulations. *Journal of Physical Oceanography*. https://doi.org/10.1175/JPO-D-18-0252.1

Wåhlin, A. K., Yuan, X., Björk, G., & Nohr, C. (2010). Inflow of warm circumpolar deep water in the Central Amundsen Shelf. *Journal of Physical Oceanography*, *40*, 1427–1434. https://doi.org/10.1175/2010JPO4431.1

Walker, D. P., Jenkins, A., Assmann, K. M., Shoosmith, D. R., & Brandon, M. A. (2013). Oceanographic observations at the shelf break of the Amundsen Sea, Antarctica. *Journal of Geophysical Research: Oceans*, *118*, 2906–2918. https://doi.org/10.1002/jgrc.20212

Walker, R. T., Dupont, T. K., Parizek, B. R., & Alley, R. B. (2008). Effects of basal-melting distribution on the retreat of ice-shelf grounding lines. *Geophysical Research Letters*, *35*, L17503. https://doi.org/10.1029/2008GL034947